

Master Thesis

Searching for the Dark Photon

by

CARINA UNGETHÜM

Supervisor: JProf. Dr. Tetyana Galatyuk

Second Advisor: Dr. Malgorzata Gumberidze

Institut für Kernphysik



TECHNISCHE
UNIVERSITÄT
DARMSTADT

May 30, 2015

Suche nach dem Dunklen Photon
Searching for the Dark Photon

Vorgelegte Master-Thesis von Carina Ungethüm

1. Gutachter: Prof. Dr. Tetyana Galatyuk
2. Gutachter: Dr. Malgorzata Gumberidze

Tag der Einreichung:

Zusammenfassung

In der vorliegenden Arbeit werden die Au+Au Kollisionen, mit einer kinetischen Strahlenergie von 1.23 AGeV gemessen von dem **High Acceptance Dilepton Spectrometer (HADES)** diskutiert und analysiert. HADES ist an dem GSI Helmholtzzentrum für Schwerionenforschung in Darmstadt installiert. Das physikalische Ziel ist die systematische Messung von Elektronen- und Positronenpaaren, sowie der Produktion von Strangeness in elementaren (pp, pA, π p, π A) und Schwerionenkollisionen. Der Hauptfokus in dieser Arbeit liegt auf der Rekonstruktion des U(1) Eichbosons im e^+e^- Zerfallskanal. Die dunkle Materie kann über ein solches U(1) Gauge Boson mit der sichtbaren Materie wechselwirken. Das Standardmodell ist dafür mit einer zusätzlichen U(1)' Symmetrie, analog zu der U(1) Symmetrie, ausgestattet. Die kinetische Mischung zwischen den beiden Symmetrien ergibt die natürliche Verbindung von dunkler und sichtbarer Materie. Das dunkle Photon, welches der U(1)' Symmetrie zugeordnet wird soll eine Masse im Bereich MeV/c^2 bis GeV/c^2 besitzen, mit einer Breite von $\Gamma_U \ll 1 \text{ MeV}/c^2$. Solch ein Modell soll verschiedene astrophysikalische Beobachtungen, sowie die bisher nicht erklärte Differenz zwischen dem theoretischen und gemessenen magnetischen Moment des Myons erklären. Die Leptonen werden mittels eines neuronalen Netzwerkes identifiziert. Damit lässt sich die Effizienz nach den Identifikationsschnitten deutlich verbessern. Die Reinheit des Leptonensatzes steigt auf über 95% an. Es werden verschiedene Zusammensetzungen der Eingangsvariablen für das neuronale Netzwerk getestet und mit den Ergebnissen aus den Simulationsdaten verglichen. Es zeigt sich, dass es hinsichtlich Effizienz und Reinheit der Leptonen von Vorteil ist die Information über den Impuls und den polaren Winkel θ für das Training des Netzwerkes beizubehalten. Es zeigt sich, dass es vorteilhaft ist die Information über den Impuls und den polaren Winkel der rekonstruierten Spur beizubehalten. Wird die Information über den polaren Winkel nicht genutzt, fällt die Effizienz nach Identifikationsschnitten von 19% auf 14%. Die e^+e^- Paare werden anschließend aus den einzelnen Leptonen zusammengesetzt und das resultierende Spektrum wird für die Suche nach dem Dunklen Photon verwendet.

In dieser Arbeit wird nach einem Zerfall des dunklen Photons in e^+e^- Paare, im Dileptonen Spektrum gemessen bei der Au+Au (1.23 AGeV) Kollision, gesucht. Ein oberes Limit für den Parameter der kinetischen Mischung bei einem Konfidenzintervall von 90% ist bis zu einer invarianten Masse von $0.55 \text{ GeV}/c^2$ bestimmt worden und mit den Daten anderer Experimente abgeglichen. Darüber hinaus wird eine neue Methode für das Matching zwischen dem rekonstruierten Spur aus MDC und den x- und y-Koordinaten aus dem Flugzeitdetektor vorgestellt. Der Vorteil ist, dass man die Punktgenaue Spurrekonstruktion aus den MDC nutzen kann.

Abstract

In this thesis the analysis of Au+Au collisions, with kinetic beam energy of 1.23 AGeV, measured with the **H**igh **A**cceptance **D**ilepton **S**pectrometer (HADES) is discussed. HADES is located at the GSI Helmholtzzentrum für Schwerionenforschung in Darmstadt. The physics goals are the systematic measurement of electron-positron pairs and strangeness produced in elementary (pp, pA, π p, π A) and heavy-ion collisions.

The main focus of this thesis is on the reconstruction of U(1)-gauge boson in e^+e^- decay channel. The dark matter can interact with the visible matter via a U(1) gauge boson, the so called U-boson (A' , γ' or dark photon). The Standard Model of particle physics is thereby supplemented with an additional sector characterized by the U(1)' symmetry, which is the counterpart to the SM U(1) symmetry. The kinetic mixing of the U(1) and U(1)' symmetry groups gives a natural connection between the SM and Dark Matter (DM). The dark photon is constrained to be in the MeV/c^2 to GeV/c^2 range and should have a small width of $\Gamma_U \ll 1 \text{ MeV}/c^2$. Such models are also proposed to explain some recent puzzling astrophysical observations, as well as to solve the so far unexplained deviation between the measured and calculated values of the muon anomaly. The leptons are identified using a neural network approach. By using the neural network one can gain in efficiency after applying identification cuts. The purity of the lepton sample can be pushed up to be larger than 95%. For the set of input variables for the neural network different opportunities have been tested and compared with simulation results. It turns out that it is useful to keep the information about the particle momentum and the polar angle of the track as an input variable for the training of the multivariate analysis. I.e. if the information of the polar angle is used for the training, the efficiency after applying identification cuts increases from 14% to 19%. The e^+e^- pairs are built up of the identified leptons. The resulting inclusive dilepton spectrum is further used for searching for the dark photon. In the thesis a search for the e^+e^- decay of such a hypothetical dark photon in the inclusive dielectron spectra measured by HADES in the Au (1.23 GeV) + Au reaction is presented. An upper limit on the kinetic mixing parameter at 90% CL has been obtained for a mass range lower than $0.55 \text{ GeV}/c^2$ and is compared with the present world data set. In addition the new way of matching a track reconstructed in MDC to the x- and y-coordinate reconstructed in the time-of-flight system is discussed. The main advantage of this method lies in the fact that it allows to take advantage of using pointing accuracy provided by the track reconstruction in MDC.

Contents

1	Motivation	9
2	The Dark Photon	11
2.1	Astrophysical Observations	11
2.2	Standard Model and its Extensions	12
2.3	Experimental Search for Dark Photon: Status and Plans	13
3	The HADES Spectrometer	15
3.1	The detector system	17
3.1.1	Start and Veto detector	17
3.1.2	Ring Imaging Cherenkov detector	17
3.1.3	Low-mass Multiwire Drift-Chambers	18
3.1.4	Multiplicity and Electron Trigger Array Detectors	20
3.1.5	The Forward Wall	22
3.2	Experimental Program	22
4	Analysis Framework	25
4.1	PLUTO Event Generator	25
4.2	UrQMD	25
4.3	HGEANT	25
4.4	HADES System for Data Reduction and Analysis	26
4.5	Toolkit for Multivariate Data Analysis	26
4.6	Computation of Confidence Intervals using TRolke	29
5	Analysis of the Au+Au Data	31
5.1	Use of the MLP Network for Electron Identification	32
5.1.1	Validations with Simulation Data	40
5.2	Correction of META dx in the TOF region	44
5.3	Inclusive Dilepton Spectrum	48
5.3.1	Calculation of the Combinatorial Background	48
5.3.2	Efficiency Corrections	49
5.3.3	Acceptance Corrections	53
6	Search for the Dark Photon	57
6.1	Determination of the Upper Limit	58
6.2	Upper Limit on ϵ^2	59

7 Summary and Outlook	63
7.1 Summary	63
7.2 Outlook	63
List of Figures	65
List of Tables	69
Bibliography	71

Chapter 1

Motivation

In recent years several experiments have made striking constraints on cosmological parameters. For example measurements performed by Wilkinson Microwave Anisotropy Probe (WMPA), a NASA explorer mission that launched in 2001, allowed to constrain the age of the universe to be $13.8 \cdot 10^9$ years old and the composition of matter in the universe to be 4.5% baryonic or visible matter, while the rest consists of 22.6% of dark matter and of 72.9% of dark energy [1]. Dark matter is not interacting with the known electromagnetic force, i.e. it does not absorb, emit light or other electromagnetic radiation, which makes its direct detection impossible. The particles are arranged into two main groups in the Standard Model, leptons and quarks. In addition four particles, which are acting as force carriers, are included. The so-called “dark photon”: a particle beyond the well known Standard Model of particle physics, which carries the strong, weak and electromagnetic interactions was predicted. The question remains: how to experimentally detect “dark photon”? It is well possible that there are a lot of interesting physics going on in the dark sector, unfortunately it is too tiny for us to have noticed it. Although we do not have firm conclusions, we could provide upper limits on existence of “dark photon”.

Structure of the Present Thesis

There are two main parts of this thesis. Part one describes the experimental apparatus of HADES and analysis of Au+Au data, while part two develops the analysis of the “dark photon” search.

After an introduction about the dark photon and the HADES detector and experimental program, a method for lepton identification is presented. The experimental results are further compared with the simulation data. The corresponding dilepton spectrum is then used to search for the dark photon and to determine an upper limit of its existence.

Chapter 2

The Dark Photon

2.1 Astrophysical Observations

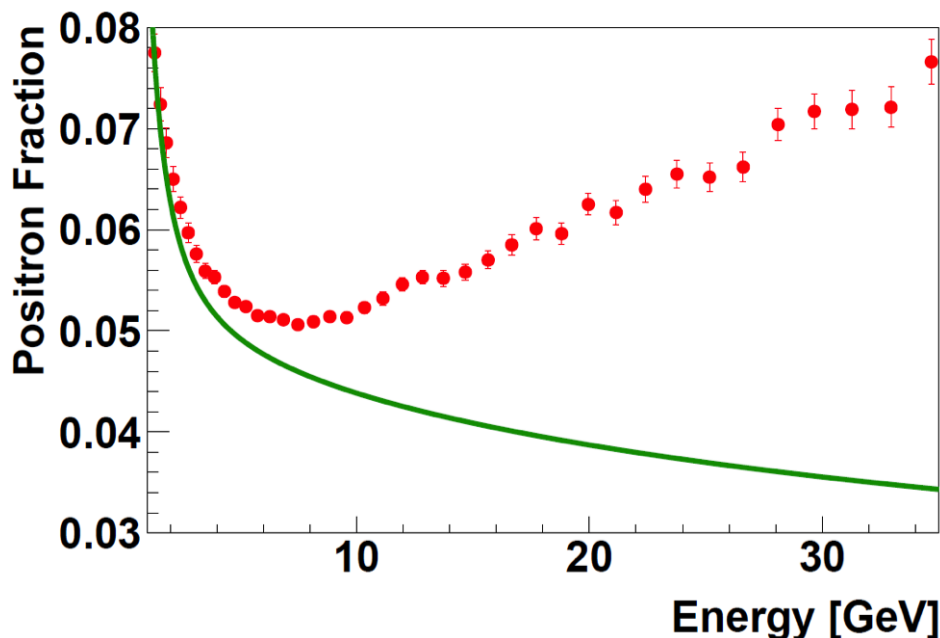


Figure 2.1: The positron fraction measured by AMS (red circles) compared with the expectation from the collision of ordinary cosmic rays showing that above 8 billion electron volts (8 GeV) the positron fraction begins to quickly increase. This increase indicates the existence new sources of positrons [2].

The astrophysical observations from different collaborations reported evidences for existence of dark matter. For example an excess of the e^+e^- annihilation γ quanta from the galactic center observed by the INTEGRAL satellite [3], the excess in the cosmic ray positron fraction $e^+/(e^-+e^+)$ reported by PAMELA [4] and more recently by AMS-02 [5] (see Fig. 2.1), the total electron and positron flux measured by ATIC [6], Fermi-LAT [7] and H.E.S.S. [8], and the annual modulation of DAMA/ LIBRA signal [9]. All these observations have failed to find an interpretation in the frame of the standard model (SM) or from particle physics sources. The alternative theoretical explanations have been proposed as an explanation for some of these anomalies. These explanations include in particular the possibility that dark matter (DM) par-

ticle annihilation could be responsible for the observed excess. The simplest scenario for DM particles postulates an additional gauge symmetry as an extension of the SM [10].

2.2 Standard Model and its Extensions

The standard model, which is a quantum field theory, based on the symmetry group $SU(3) \otimes SU(2) \otimes U(1)$. Local gauge invariance requires the existence of vector bosons mediating the strong and electroweak forces: the gluons, photon, W and Z bosons. Furthermore the SM consists out of fundamental particles such as quarks and leptons which are interacting via exchange of force carrier particles, the gauge bosons. All particles are displayed in Fig. 2.2. The elementary particles are getting the mass by interacting with the so-called Higgs boson.

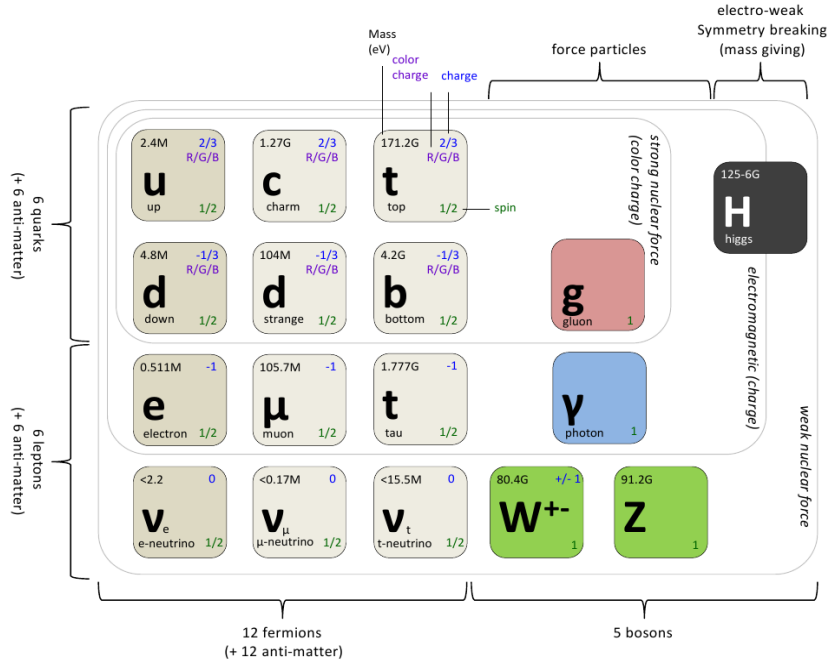


Figure 2.2: Elementary particles and force carriers of the Standard Model.

Evidences for such a boson are found at CERN by CMS [11] and ATLAS [12] Collaboration. Currently the best description for the subatomic world is the SM, but it does not explain the complete picture. As it has been mention in Sec. 2.1 extention of the SM has been proposed (more informations about the SM can be found in [13]).

Therefore the SM is supplemented with an additional $U(1)'$ gauge symmetry. The new corresponding vector gauge boson, called U boson, Dark Photon, A' or γ' , would thereby mediate the annihilation of Darm Matter (DM) into charged lepton pairs. The kinetic mixing of the $U(1)'$ and $U(1)$ symmetry will give a natural connection between the DM and the SM. For completeness the effective Lagrangian [14], which mixes the dark photon (A') with the SM photon is expressed by

$$\mathcal{L}_{eff} = \mathcal{L}_{SM} - \frac{1}{4} F'_{\mu\nu} F'^{\mu\nu} + \frac{1}{2} \epsilon F'_{\mu\nu} F^{\mu\nu} + \frac{1}{2} m_A^2 A'_\mu A'^\mu \quad (2.1)$$

with the SM Lagrangian \mathcal{L}_{SM} , the gauge kinetic term $\frac{1}{4} F'_{\mu\nu} F'^{\mu\nu}$, the term $\frac{1}{2} m_A^2 A'_\mu A'^\mu$ for small masses and the kinetic mixing term $\frac{1}{2} \epsilon F'_{\mu\nu} F^{\mu\nu}$, which expresses the mixing with the SM.

$F'_{\mu\nu}$ is thereby the dark photon field and $m_{A'}$ the dark photon mass.

To represent the interaction between SM and DM the kinetic mixing parameter ϵ is introduced, which is defined over the ratio between the coupling constants of the DM (α') and SM (α):

$$\epsilon^2 = \frac{\alpha'}{\alpha} \quad (2.2)$$

and it is expected to be of an order of 10^{-2} to 10^{-8} [15], whereas the mass of the U boson should be in a range of MeV to GeV with a width of $\Gamma \ll 1$ MeV [16].

2.3 Experimental Search for Dark Photon: Status and Plans

In recent years various experiments have performed search of the dark photon in a few-GeV beam energy regime. Such Collaborations as A1 [17] and APEX [18] have searched for the dark photon in e^+e^- pair distributions produced in electron scattering, whereas WASA-at-COSY Collaboration has looked at the pairs in the electromagnetic decay of the neutral pion. The WASA-at-COSY [19] Collaboration has covered the mass range $m_{A'} = 0.02 - 0.1$ GeV/c² by investigating the π^0 decay in proton induced reactions at 0.55 GeV beam energy.

The KLOE-2 Collaboration [20, 21] has searched instead for the hypothetical $\phi \rightarrow \eta + U \rightarrow 3\pi e^- e^+$ decay in e^+e^- collisions by analyzing the decay $\eta \rightarrow \pi^+ \pi^- \pi^0$. The latest result has come from the BaBar Collaboration [22] and from the NA48/2 Collaboration [23]. They were searching for the U boson in the $e^+e^- \rightarrow \gamma A'$ ($A' \rightarrow e^+e^-, \mu^+\mu^-$) reaction and in the π^0 decay. By setting a confidence level of 90% they are getting an upper limit on the mixing parameter of the order of 10^{-3} to 10^{-4} for a mass range from 0.02 GeV/c² to 10.2 GeV/c². The upper limit on the mixing parameter ϵ is presented in Fig. 2.3. In addition the $(g-2)_\mu$ 2σ and $(g-2)_e$ 3σ band are shown.

The $(g-2)_\mu$ constraints are a consequence of the comparison between the experimental determined anomalous gyromagnetic factor $(g-2)$ of the muon and the SM calculations [24].

$$\alpha_\mu^{exp} = 11659208.9(5.4)(3.3) \cdot 10^{-10} \quad (2.3)$$

$$\alpha_\mu^{SM} = 116591802(2)(42)(26) \cdot 10^{-11} \quad (2.4)$$

$$\Delta\alpha_\mu = \alpha_\mu^{exp} - \alpha_\mu^{SM} = 287(63)(49) \cdot 10^{-11} \quad (2.5)$$

By mixing with the ordinary photon, the dark photon couples to charged particles with the strength $\epsilon \cdot e$ and gives a contribution to the muon anomalous magnetic moment. This might explain the discrepancy between the experimental and the calculated value.

As mentioned in Chap. 1 the Au (1.23 AGeV) + Au data taken with the HADES spectrometer could lead to a new upper limit, which would confirm by independent measurement the determined upper limit from the NA48/2 or BaBar Collaborations in the mass region below $m_{A'} < 50$ MeV/c².

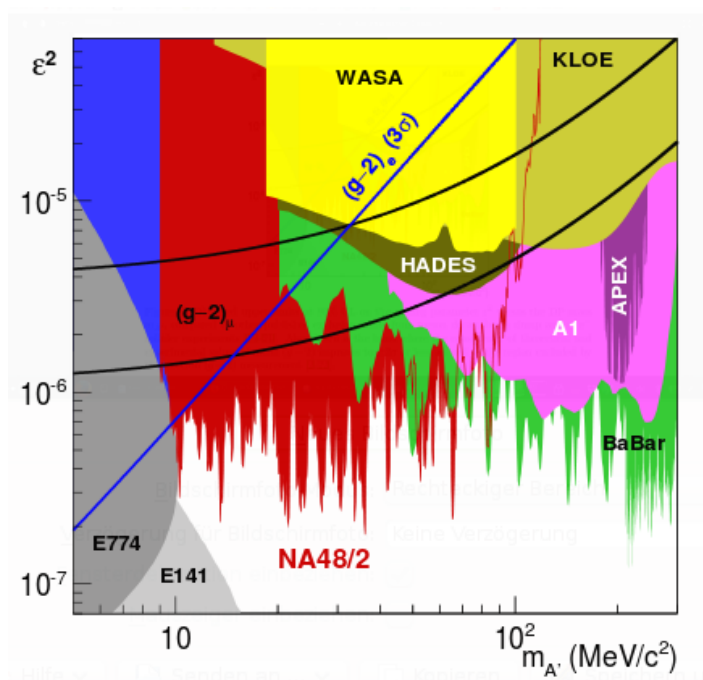


Figure 2.3: Exclusion plot at 90% CL on ϵ^2 as function of $m_{A'}$. The result from HADES [25] is compared with existing limits from the APEX [18], WASA-at-COSY [19], KLOE-2 [20, 21], BaBar [22], MAMI/A1 [26] and NA48/2 [23] experiments, as well as with the $(g-2)_\mu$ and $(g-2)_e$ constraints.

Chapter 3

The HADES Spectrometer

The goal of the heavy-ion experiments at LHC, RHIC, SPS, BEVALAC and SIS is to explore the phase structure of strongly interacting matter, which is governed by the laws of Quantum Chromo Dynamics, by creating hot and dense matter in the laboratory. When nuclear matter is heated or compressed the initially confined quarks and gluons start to be liberated. The phase transition to a quark-gluon plasma is indicating a chiral symmetry restoration. Even before the first order deconfinement phase transition is reached, the chiral symmetry is partially restored.

Various states of a matter can be accessed by selection of different collision systems and energies, as schematically presented in Fig. 3.1. For heavy-ion collisions in the energy range between 1 and 2 AGeV available at SchwerIonen Synchrotron facility (SIS), at GSI Helmholtzentrums für Schwerionenforschung, a baryon density of 3-4 times larger than the normal nuclear density and temperatures of the order of 100 MeV can be produced in a fireball with a mean lifetime of $\tau \sim 10$ fm/c [27].

As shown in Fig. 3.1 as a dashed curve, the phase transition between hadron gas and quark-gluon plasma, where quarks and gluons become deconfined, is expected at $T \sim 160$ MeV for $\mu_B=0$ as predicted by the lattice QCD [30]. The chemical freeze-out points in the diagram refers to the stage where the fireball acquires its final particle composition. According to that the thermal freeze-out marks the stage, where the final momenta of the particles are fixed.

At SIS energies both freeze-out curves are merging. The matter is clearly in the confinement region. On the other hand at density up to $\rho \approx 3 \rho_0$ a trend towards the chiral symmetry restoration is noticeable (see orange gradient in Fig. 3.1).

Lepton pairs are the good probe for the chiral symmetry restoration. Dileptons are interacting with matter only electromagnetically and therefore they carry informations of the hot and dense stage of the fireball to the detector. Dileptons are produced in the hot stage via the decay

meson	mass (MeV/c ²)	width (MeV/c ²)	lifetime τ (fm/c)	e ⁺ e ⁻ branching ratios
ρ	768	152	1.3	4.4×10^{-5}
ω	782	8.43	23.4	7.2×10^{-5}
ϕ	1019	4.43	44.4	3.1×10^{-5}

Table 3.1: Characteristic quantities of light vector mesons [29].

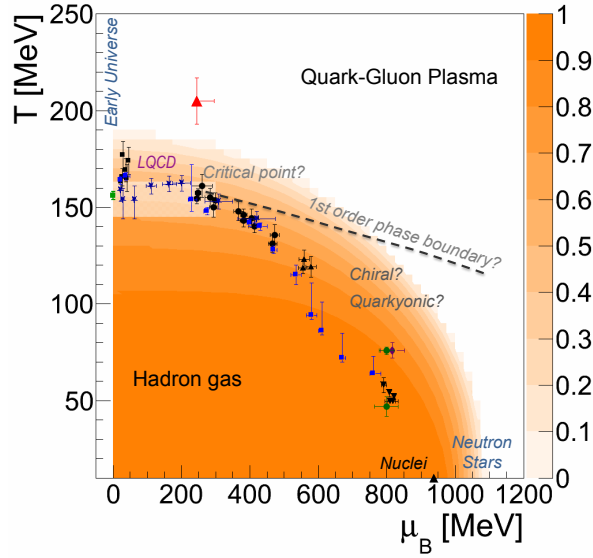


Figure 3.1: The phase diagram of QCD including data points in T and μ_B describing the final hadron ratios in a statistical model. The hadrochemical freeze-out points are determined from a thermal model analysis of heavy-ion collision data at SIS, AGS, SPS and RHIC energies. The condensate ratio $\langle q\bar{q} \rangle_{T, \mu_B} / \langle q\bar{q} \rangle_{T=0, \mu_B=0}$ in dependence on T and μ_B is shown as 3rd dimension in color code. The condensate ratio is reduced for high T and μ_B as predicted by Nambu Jona Lasinio model [28].

of vector mesons like ρ , ω and ϕ . Due to the fact that the branching ratios of the main decay are very small and one has to deal with a large background originating from π^0 -Dalitz decays and γ conversion on the detector materials, the electromagnetic decay of the vector mesons are complicated probes. Furthermore the observed dilepton spectrum consists of leptons coming from different stages of the fireball, which makes the interpretation of the result more difficult.

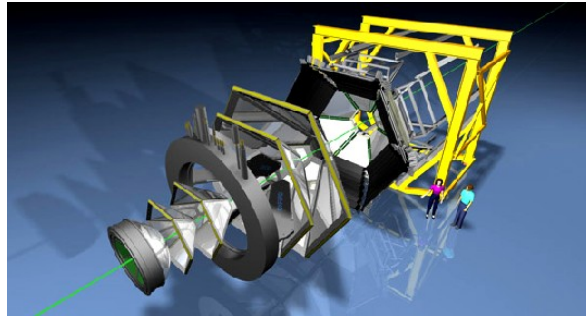


Figure 3.2: Overview over the HADES spectrometer [31].

The **H**igh **A**cceptance **D**ilepton **S**pectrometer is placed at GSI Helmholtzzentrum für Schwerionenforschung Darmstadt. It is constructed for detection of e^+e^- pairs and charged hadrons. The ring accelerator SIS 18 [32] provide protons and heavy-ion beams (up to uranium) to a fixed target. Secondary pion beams can be delivered from a production target to the HADES target as well. The spectrometer is arranged into six symmetric sectors surrounding the beam axis with nearly 360° azimuthal coverage. A cross section of the complete spectrometer is shown in Fig 3.3.

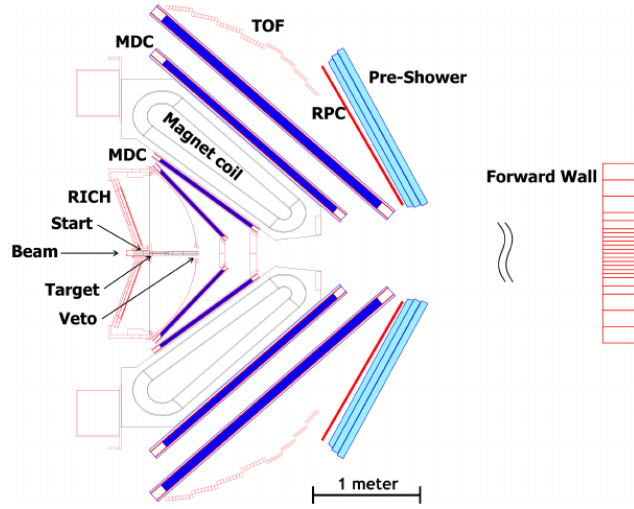


Figure 3.3: Cross-section of the HADES with the different detector components shown [33].

For an efficient identification of dileptons the experimental setup has to fulfill the following requirements:

- high invariant mass resolution (few %),
- large geometric acceptance,
- trigger system optimized for high data rates [34],
- low production of secondary particles, low material budget,
- excellent discrimination of hadronic background.

The components of the HADES is explained in detail in Sec. 3.1.

3.1 The detector system

3.1.1 Start and Veto detector

The Start detector determines the time zero of the reaction (t_0). It is used for the time-of-flight measurement in order to identify particles. The Start detector is placed 2 cm in front of the target (for Au+Au at 1.25 AGeV) whereas the Veto detector is located 70 cm behind the target. For the Au+Au experiment the Start detector was built from monocrystalline diamond with a thickness of 50 μm and a surface of 4.7 x 4.7 mm^2 . The thickness was chosen to keep the interaction probability as low as possible. For diamond material with a thickness of 50 μm the interaction probability is equal to 0.26 %. The obtained time resolution is lower than 50 ps [35].

3.1.2 Ring Imaging Cherenkov detector

The Ring Imaging Cherenkov (RICH) is a gas filled detector located in the inner part of the spectrometer and is designed to identify relativistic positrons and electrons in a momentum range of $0.1 \text{ GeV}/c \leq p \leq 1.5 \text{ GeV}/c$.

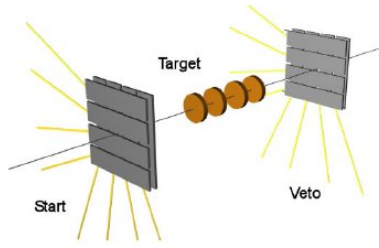


Figure 3.4: Schematic view of the start and veto detector [35].

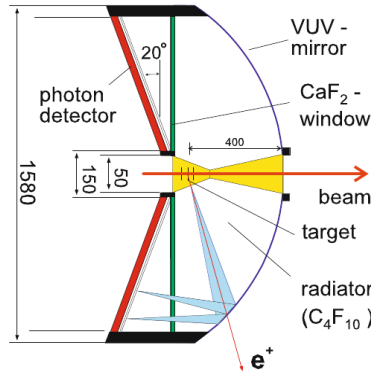


Figure 3.5: Schematic layout of the RICH, consisting of a carbon shell mirror, a CaF_2 entrance window and a photon detector. All distances are in millimeter [33].

If an e^\pm is going through the perfluorobutan (C_4F_{10}) radiator gas it produces Cherenkov radiation, whereas hadrons with a velocity of $\beta = 0.95$ are below the Cherenkov threshold of $\gamma_{th} = 18$. The emitted Cherenkov radiation is reflected by a segmented spherical VUV-mirror (diameter $\varnothing = 145\text{cm}$, curvature $R = 870\text{ mm}$ [36]) and focused onto a position-sensitive photon detector with CaF_2 entrance window to form rings of almost constant radius. With increasing polar angle of lepton tracks the Cherenkov images detected on the planar MWPC pad plane turn from rings to ellipses. A variation of the pad size depending on its position in the focal plane is used to correct the eccentricity of the ring images and leads to rings of almost constant radius of about four pads for all track angles. The gas volumes of the radiator gas (C_4F_{10}) and photon detector (CH_4) are separated by a single CaF_2 -window. The number of emitted photons is depending on the distance traversed by the electrons in the radiator gas (from 36 to 65 cm, depending on the polar angle of the particle emission) and can vary by a factor of two. All particles which are in the acceptance of the spectrometer travel through the RICH. To minimize multiple scattering and pair conversion a low material budget was chosen and the used materials were selected very carefully.

3.1.3 Low-mass Multiwire Drift-Chambers

In order to use the spectrometer for high-resolution spectroscopy of vector mesons ($\sigma_{M_\omega}/M_\omega \simeq 2.5\%$) in elementary and heavy-ion collisions via their dielectron decay channels one needs an intrinsic spatial cell resolution better than $150\ \mu\text{m}$. As mentioned before a low mass design was chosen for the tracking system. Therefore 24 trapezoidal Multiwire Drift-Chambers (MDC) are used, which are arranged in four planes, two in front of the magnet and two behind (Fig. 3.3). The detector covers a polar angle of 18° to 85° and is build up in six

identical sectors. Each chamber consists of six sense/field wire layers which are oriented in six

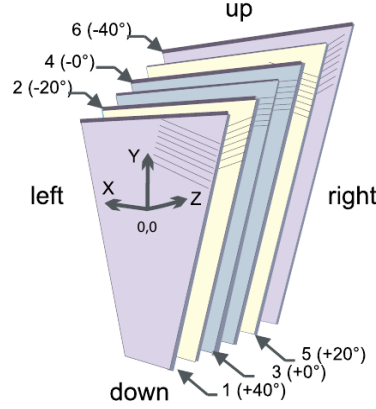


Figure 3.6: Schematic view of the six anode wire frames inside a MDC [33].

different stereo angles ($\pm 0^\circ, \pm 20^\circ, \pm 40^\circ$) in order to reach the maximum spatial resolution in polar direction, see Fig. 3.6. Each chamber contains around 1100 signal wires.

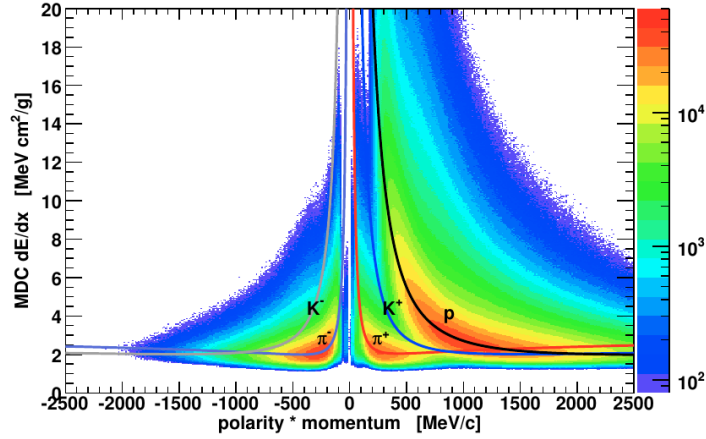


Figure 3.7: Momentum-dependent dE/dx distribution (normalized) measured by MDC. Energy loss curves of several hadron species are calculated by Bethe-Bloch formula (Eq. 3.1) and plotted into distribution [29].

When a particle passes through a drift chamber the gas in the chamber is ionized and the produced electrons are traveling to the signal wires. Close to the wire the field gradient is high enough that accelerated electrons ionize further gas atoms. This leads to the formation of a measurable signal and by using the width of the signal (**t**ime **o**ver **t**reshold, ToT) one can calculate the energy loss dE/dx of registered particles. The Bethe-Bloch formula [37] describes the energy loss of relativistic particles in matter: see eq. 3.1.

$$-\frac{dE}{dx} = 4\pi N_A r_e^2 m_e c^2 z^2 \frac{Z}{A} \frac{1}{\beta^2} \left[\frac{1}{2} \ln \left(\frac{2m_e c^2 \beta^2 \gamma^2 T_{max}}{I^2} \right) - \beta^2 - \frac{\delta}{2} \right], \quad (3.1)$$

with z being the charge of the incoming particle, Z and A the atomic and mass number of the gas, m_e the electron mass, r_e the electron radius, N_A the Avogadro number, I the characteristic

ionization constant of the gas and δ as the density correction term. The maximum kinetic energy, passed to one electron in a single collision is given by T_{max}

$$T_{max} = \frac{2m_e c^2 \beta^2 \gamma^2}{1 + 2\gamma m_e/M + (m_e/M)^2}, \quad (3.2)$$

where M is the mass of the colliding particle. Further details about the calculation of the energy loss can be found in [31].

Between the second and third MDC plane a **IronLess Superconducting Electron Magnet (ILSE)** is positioned. The superconducting magnet is cooled down by liquid helium and produces a toroidal field. This geometry provides a field-free region around the target and inside the active volume of the RICH. At operating temperature of 4.6 K and a current of 3665 A the maximal value of the field strength is 3.7 T. The transverse momentum which is transferred to the particles traveling through the field lies between 40 MeV/c and 120 MeV/c.

3.1.4 Multiplicity and Electron Trigger Array Detectors

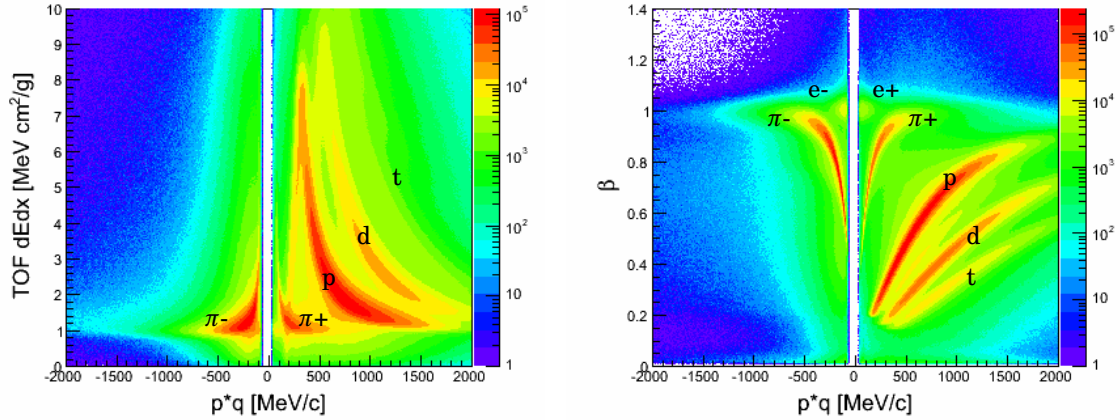


Figure 3.8: Left: Energy loss vs. momentum distribution in TOF region with identified particles. Right: β vs. momentum distribution for TOF region with identified particles.

The **Multiplicity and Electron Trigger Array (META)** is a system of three different detectors. For time-of-flight measurement, the TOF or RPC detectors are used, whereas the Pre-Shower detector is used for identifying electrons. Furthermore, the META detector provides an additional tracking point which helps to reconstruct the particle track. META is used to define the track multiplicity for each reaction. The combination of the time-of-flight measurement with momentum determination and the energy loss measurement allows an efficient particle identification (e, π , K, p, d, t and light nuclei).

Time of Flight wall

The TOF wall covers polar angles between 44° and 88° and is placed behind the tracking system. It is mainly used for triggering and particle identification. By determining the charged-particle multiplicity it allows to select certain reaction classes (first-level trigger decision). Whereas the fast determination of the impact parameter of each particle, spatially correlated with the RICH detector, provides a second-level trigger decision. As a result of the second-level trigger, only events with lepton track candidates can be selected. This possibility was not used

in the Au+Au run, since in virtually every event there is a lepton candidate.

The TOF detector consists of six sectors with eight modules. Each module is built up of eight scintillator rods. By passing through the detector material charged particles are generating excited states. While falling back to the ground state light is emitted. The light pulses are read-out by two photomultipliers attached to both sides of the rods. By measuring the height and width of the signal one can extract the energy loss of each particle. Furthermore the time of flight is measured with a resolution corresponding to $\sigma_{\text{TOF}} \approx 190$ ps in coincidence with the signal of the start detector and an intrinsic resolution of $\sigma_{\text{TOFint}} \approx 150$ ps. The velocity as a function of momentum is shown together with the energy loss vs. momentum distribution in Fig. 3.8.

RPC detector

The RPC detector, which reaches a time-of-flight resolution of 75 ps, covers the inner region of the spectrometer, 18° to 45° . It is built up of resistive plate chambers and features 372 channels per sector, which are needed in order to reconstruct high particle multiplicity in heavy ion collisions.

Pre-Shower detector

The Pre-shower detector is used in addition to the RPC detector to distinguish between fast

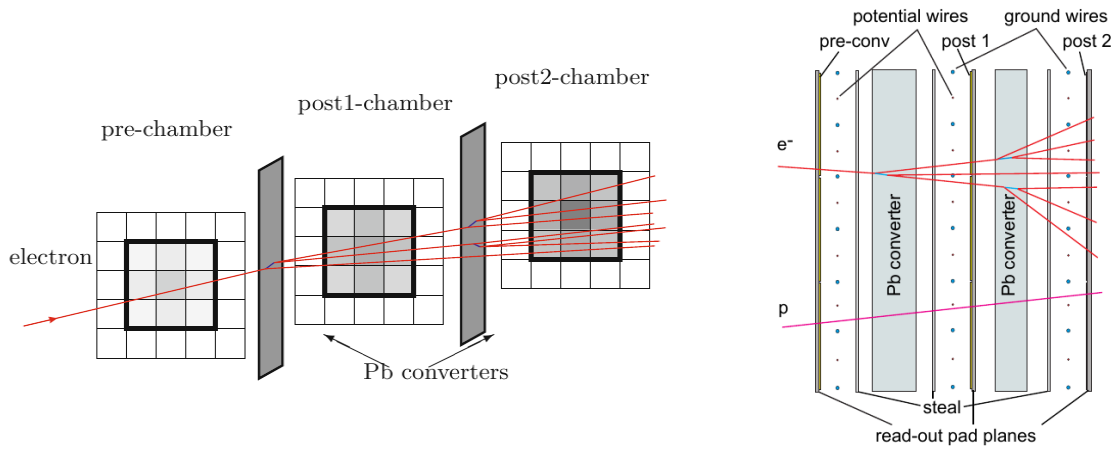


Figure 3.9: **Left:** Schematic view of the electromagnetic shower algorithm. In each layer the charge over the 3x3 pads is integrated. The large charge deposition in the post chambers is the signature of an electromagnetic shower [33]. **Right:** Schematic layout of the Pre-Shower detector [37].

pions and electrons. Each sector consists of three trapezoidal chambers (Pre, Post 1, Post 2). They are separated by Pb converter plates as shown in Fig. 3.9. If a charged particle travels through the gas chambers, the induced charge is measured on the cathode pads with an individual readout. In order to get the complete charge of the electromagnetic shower the charge is integrated on several pads around the one with the highest local charge deposition (Fig. 3.9). The integration is also done over all three corresponding layers. The shower signal

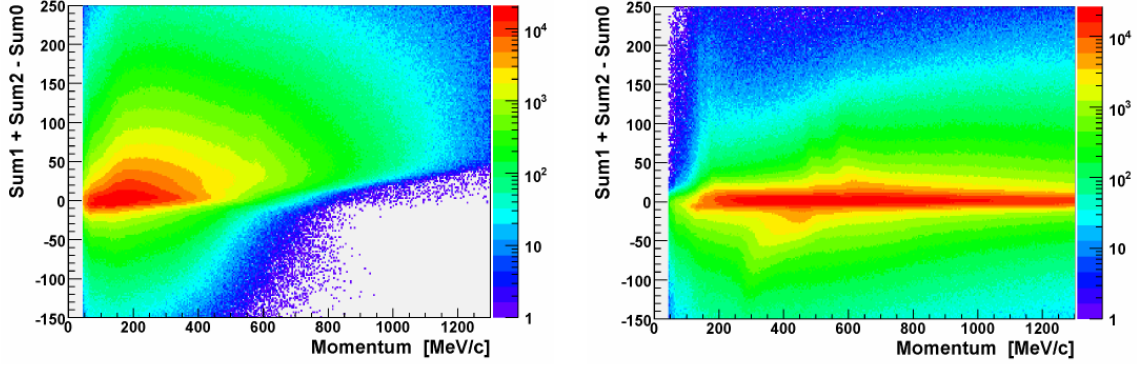


Figure 3.10: Pre-Shower signal of leptons (left) and hadrons (right).

is calculated as

$$\Delta Q = Q_{\text{SUM1}} + Q_{\text{SUM2}} - Q_{\text{SUM0}} \quad (3.3)$$

where the index 0 belongs to the entry chamber and 2 to the exit chamber. The shower signal for leptons and hadrons is plotted in Fig. 3.10.

3.1.5 The Forward Wall

The Forward Wall is a hodoscope, which covers a polar angle below 7° [38]. It is built up of 287 scintillator blocks with a cell sizes from 4 cm x 4 cm up to 16 cm x 16 cm depending on the expected particle flux. The hodoscope is placed 7 m behind the target and provides measurement of spectators. The Forward Wall is used to determine the event plane and serve as a centrality selection detector.

3.2 Experimental Program

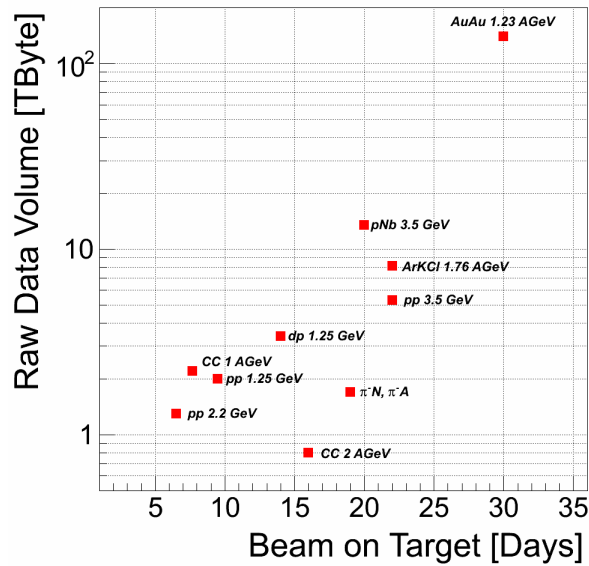


Figure 3.11: Recorded raw data as a function of the beam on target for different experiments.

Between 2002 and 2014 various collision systems at different beam energies have been investigated at HADES. The full list of experiments is given in Tab. 3.2. The first run with

Year	System	Energy	Events (rec./LVL1)	Events (rec./LVL2)
2002	C + C	2 AGeV	$0.2 \times 10^9 / 0.6 \times 10^9$	
2004	C + C	1 AGeV	$0.6 \times 10^9 / 1.1 \times 10^9$	
2005	A + KCl	1.765 AGeV	$0.9 \times 10^9 / 2.2 \times 10^9$	
2006	p + p	1.25 GeV	0.9×10^9	
2007	p + d	1.25 GeV	2.0×10^9	
2007	p + p	3.5 GeV	1.1×10^9	
2008	p + Nb	3.5 GeV	4.4×10^9	
2012	Au + Au	1.23 AGeV		4.7×10^9
2014	$\pi^- + N / \pi^- + A$	0.656 - 1.7 GeV/c		0.8×10^9

Table 3.2: This list of experiments with different collision systems and beam energies have been conducted using the HADES spectrometer. The number of events recorded is shown. The number of LVL1 triggers is given [34].

C+C at 1 AGeV and 2 AGeV was to confirm results which have been collected by the DLS Collaboration [39]. The medium-sized system Ar+KCl [40] allows to draw conclusions on the of virtual photons radiation from baryon dominated fireball and strangeness production and propagation in dense matter was taken in 2005. In 2008 an experiment on cold nuclear matter at saturation density was done with p+Nb reactions [41]. Measurements with p+p and n+p reactions were performed in 2006 (p+p at 1.25 GeV) [42] and 2007 (p+d at 1.25 GeV and p+p at 3.5 GeV) and serve as a reference spectra for studying in-medium effects. In 2012 the heaviest system (Au+Au) at a maximum available at SIS 18 energies of 1.23 AGeV has been measured. In 2014 it was the first time when pions were produced in a production target and the secondary beam reacts later with the reaction target (carbon, tungsten or polyethylene). Pion induced reactions were also measured at different beam momenta. A dilepton spectrum measured by the HADES spectrometer in p+p reactions at 3.5 GeV is shown in Fig. 3.12. In addition a simulated cocktail produced with a PYTHIA event generator is plotted for comparison with the measured data in the vector meson region, a distribution peak corresponding to direct ω decays was reconstructed with a mass resolution of 2 %.

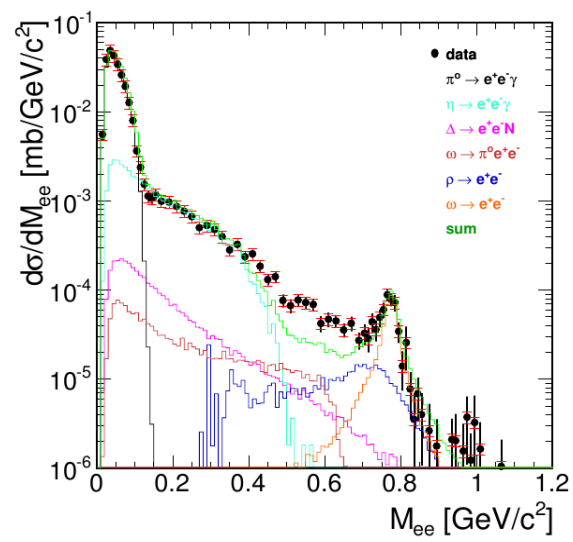


Figure 3.12: The HADES data for the $p(3.5 \text{ GeV}) + p \rightarrow e^+e^- X$ reaction from 2007, compared to a simulated cocktail from the PYTHIA event generator [43].

Chapter 4

Analysis Framework

4.1 PLUTO Event Generator

The ROOT [44] based event generator Pluto [45] is developed to simulate in an easy way hadron decays in proton-proton, proton-nucleon and nucleon-nucleon collisions. It is used as an input source for the HGEANT simulation [46].

4.2 UrQMD

The **U**ltrarelativistic **Q**uantum **M**olecular **D**ynamics model [47] is a microscopic transport model to simulate relativistic heavy ion collisions. It helps to gain understanding of the following physical phenomena:

- creation of dense hadronic matter at high temperatures,
- properties of nuclear and resonance matter,
- creation of mesonic matter and anti-matter,
- creation and transport of rare particles in hadronic matter,
- creation and transport of strangeness in matter,
- emission of electromagnetic probes.

UrQMD transport model is typically used to simulate the hadronic and photonic background. e^+e^- signal from Pluto is then embedded of event by event basis to UrQMD event.

4.3 HGEANT

The passage of charges particles through HADES is simulated by HGEANT [46], which is written in FORTRAN and built upon the GEANT [48] program . HGEANT takes the information from the event generator and tracks the particles through the detector material. Various physics processes are included in GEANT. Particles, like leptons, hadrons and π , are included.

4.4 HADES System for Data Reduction and Analysis

The HYDRA [49] framework, which is based on ROOT C++ classes, is used for HADES on-line and offline analysis and is developed by the collaboration. The ROOT software package, which is developed and maintained at CERN, provides users several built-in features and is accepted as a standard tool in high energy and nuclear physics. In HADES all necessary detector parameters are stored in the Oracle database [50], where the full version management is available.

4.5 Toolkit for Multivariate Data Analysis

In present analysis lepton identification is based on a multivariate analysis. For this propose package TMVA [51] implemented into ROOT framework is used.

In a first step one has to decide which variables are important and necessary to define signal and background sample in the multivariate analysis. With these variables one produces a sample of correlations called weight. The background includes mainly hadrons, whereas the signal ideally should consist of leptons. We define the signal and background sample based on spatial correlations between RICH ring (θ_{Ring} , ϕ_{Ring}) and track ($\theta_{Runge-Kutta}$, $\phi_{Runge-Kutta}$) provided by Runge-Kutta track fitter. To do so one uses experimental information. The same number of signal particles and background particles are used. The variable richQa is defined as

$$\text{richQa} = \sqrt{\Delta\phi^2 \sin^2\theta + \Delta\theta^2}. \quad (4.1)$$

Where ϕ_{Ring} is the azimuth angle and θ_{Ring} the polar angle. Combined with the angle out of the Runge-Kutta method one gets

$$\Delta\theta = \theta_{Ring} - \theta_{Runge-Kutta} \quad (4.2)$$

$$\Delta\phi = \phi_{Ring} - \phi_{Runge-Kutta} \quad (4.3)$$

The smaller the value of richQa, the better the pointing of the track to the ring center is. Large values of richQa signals a random match. Therefore we use $\text{richQa} < 0.5^\circ$ to define the signal and $\text{richQa} > 7^\circ$ to define the background. In Fig. 4.1 the richQa value is plotted as a function of momentum. To cut on a richQa value of 0.5° for the signal sample makes sure that all wrong

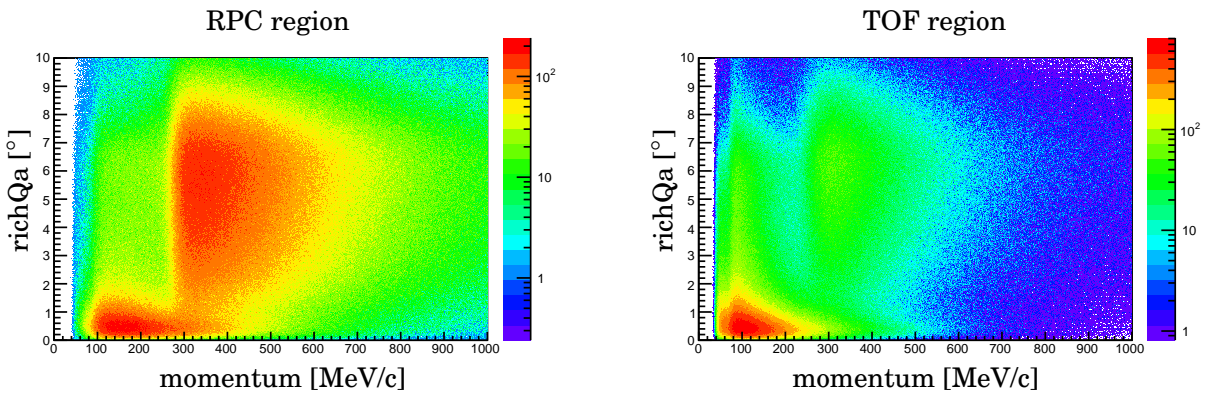


Figure 4.1: RICH matching quality (richQa) as a function of momentum based on the experimental data in RPC and TOF region.

matched track-rings are sorted out.

After all the weights are defined one puts them to the multivariate analysis tool and process the data. As a result MVA gives a scalar response answering whether the particle candidate belongs to the signal or to the background.

Multi-Layer Perceptron Artificial Neuronal Network

Generally an artificial neuronal network is a collection of interacting neurons in which every neuron produces a response depending on the input samples. In TMVA three different neuronal networks are available [51]. For our purpose the newly developed neuronal network MLP is the best choice because it is faster and more flexible than the other two. In Fig. 4.2 and Fig. 4.3 the neuronal network is shown schematically. Only the input and output layers are visible. Behind every neuron one has a characteristic propagation coefficient with its own weighting coefficient. The computing time is proportional to the number of neurons. To avoid a long computing time it is necessary to use more than one hidden layer.

A synthetic neuron at the position k in the layer l with n neurons in the input layer with there particular output value x_i is represented by

$$\text{neuron}^{(k,l)} = a^{(k,l)} \cdot s \quad (4.4)$$

$$a^{(k,l)} = w_0^{(k,l)} + \sum_{i=0}^n w_i^{(k,l)} x_i \quad (4.5)$$

$$s = \frac{1}{1 + e^{-ta}} \quad (4.6)$$

which is the standard setting of the toolkit. $a_{(K,L)}$ is the output value of the neuron, s represents the sigmoid response function, $w_i^{(K,L)}$ the weighting coefficients produced by the training procedure and $w_0^{(K,L)}$ as a summand which defines a certain output range for the network (in our case between 0 (background) and 1 (signal)).

To get the final weighting coefficients from the training, the TMVA software runs through the following scheme:

1. Initialising of random weighting coefficients.
2. Inserting all N vectors \vec{x} of the training sample in the network. Comparison of the current response value y_{current}^i with the desired value $y_{\text{desired}} \in 0,1$, which produces following error:

$$E(\vec{x}_0, \dots, \vec{x}_N | \vec{w}) = \sum_{i=0}^N \frac{1}{2} (y_{\text{ist}}^i - y_{\text{soll}})^2 \quad (4.7)$$

3. Modification of the weighting coefficients \vec{w}^{e+1} by a small change η in the direction $-\nabla_{\vec{w}} E$ for the next training cycle

$$\vec{w}^{e+1} = \vec{w}^e - \eta \nabla_{\vec{w}} E \quad (4.8)$$

4. Shuffling of the sample data to avoid a learning procedure of the neuronal network concerning the sample order.
5. Finally after a several training cycles one gets the final weighting coefficients.

After the training one can apply the weights to the data. As a result one get the so-called MLP response between 0 and 1, on which one can apply a sharp cut. In the following investigations one applies a cut on the MLP reponse larger than 0.6 (see chap. 5).

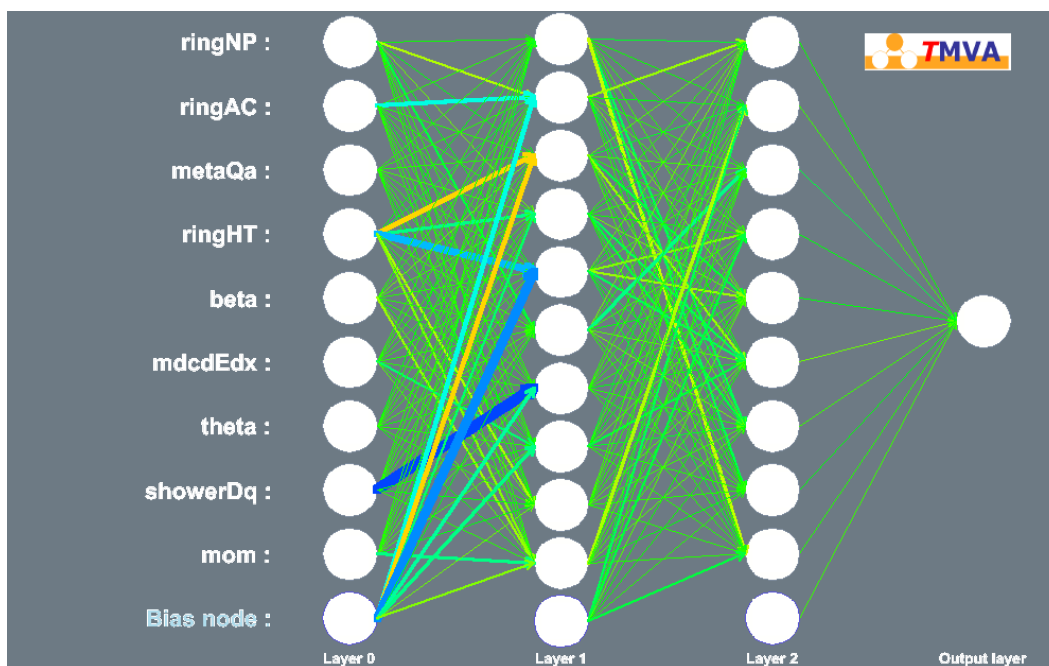


Figure 4.2: Architecture of the neural network used for the Au+Au data analysis in the region of the RPC detector. Shown are couplings between the neurons of the input layer (0), the two hidden layers (1,2) and the output layer.

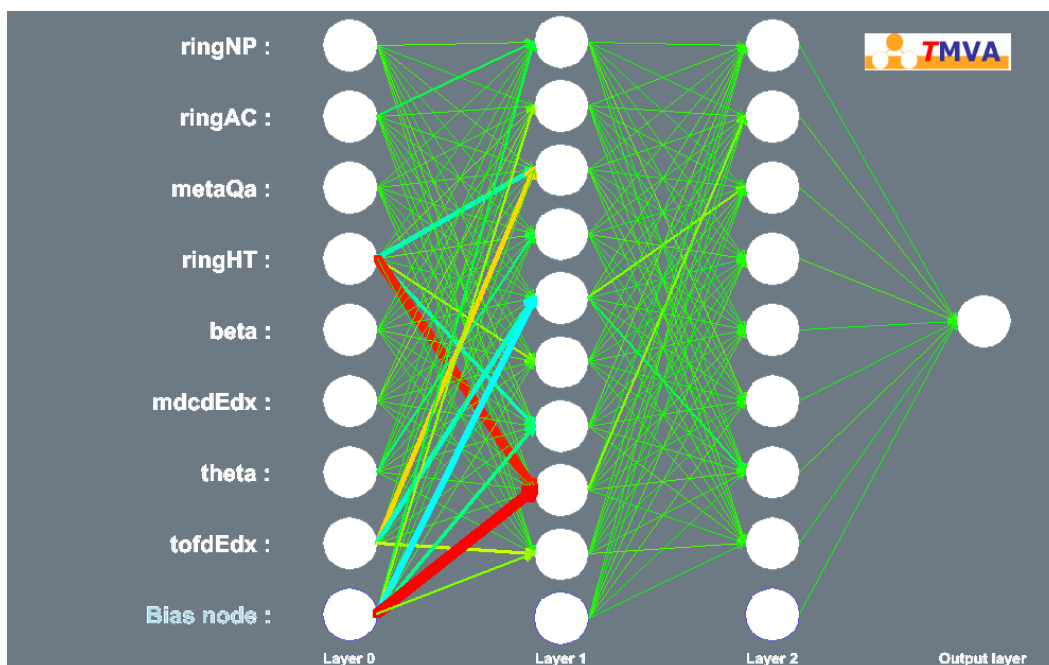


Figure 4.3: Architecture of the neural network used for the Au+Au data analysis in the region of the TOF detector. Shown are couplings between the neurons of the input layer (0), the two hidden layers (1,2) and the output layer.

4.6 Computation of Confidence Intervals using TRolke

To put an upper limit on the U-boson mixing parameter ϵ^2 the C++ based TRolke class is used. TRolke 2.0 was published in 2010 by J. Lundberg, J. Conrad, W. Rolke and A. Lopez [52]. It is implemented in the ROOT framework and was written for the calculation of frequentist confidence intervals using the profile likelihood method.

Before going into details one should discuss the so called profile likelihood method. The frequentist limit is calculated from given data in such a way that when repeated with new data the limit covers the fixed but unknown parameter with a frequency which converges to the requested probability, which is called the confidence level $1-\alpha$. The profile likelihood method represents the standard procedure for computing a confidence level and is based on the inversion of a hypothesis test. A classical hypothesis test investigates the validity of a default hypothesis. The null hypothesis \mathcal{H}_0 means that an examined sample of data is compatible with background, whereas the complementary hypothesis \mathcal{H}_1 stands for a discovery. Let us assume that one has an observable X , which we are interested in, with a probability density function $f(X_i | \pi, b)$ depending on k parameters $\pi = (\pi_1, \pi_2, \dots, \pi_k)$, as strength of different signal sources, and l additional nuisance parameters $b = (b_1, b_2, \dots, b_l)$ as strength of different background sources. For a given set of n independent observations $X = (X_1, X_2, \dots, X_n)$ the likelihood is

$$L(\pi, b | X) = \prod_{i=1}^n f(X_i | \pi, b). \quad (4.9)$$

Moreover, the likelihood ratio test statistic is defined as

$$\lambda(\pi_0 | X) = \frac{\sup\{L(\pi, b | X); \pi = \pi_0, b\}}{\text{sub}\{L(\pi, b | X); \pi, b\}}, \quad (4.10)$$

in which the denominator is the likelihood maximized over the whole $\{\pi, b\}$ space, whereas the nominator is maximized over the more restrictive null hypothesis space $\{\pi = \pi_0, b\}$. The likelihood ratio λ is known as the so called profile likelihood, which is dependent on the data. In order to determine the confidence region, one has to scan over all possible signals which is done for the U-boson in Chap. 6. The statistical performance of the profile likelihood method and more details can be found in [52].

In the case of a null hypothesis test, as one uses for the U-boson, of course the analysis has to be optimized for getting an optimal limit setting power. The upper limit is an output of the method *GetLimits*(s_L, s_U). TRolke 2.0 provides seven different statistical models to calculate the upper limit. Different combinations of Binomial, Gaussian and Poissonian or no uncertainties are implemented. For the U-boson one applied a model, which uses Gaussian uncertainties for background and efficiency.

Chapter 5

Analysis of the Au+Au Data

In April-May 2012 HADES conducted a beam time of 32 days with an Au ion beam ($E_{kin} = 1.23$ AGeV) colliding on a Au target. In order to construct a dilepton spectrum one first has to identify with high efficiency and high purity all single leptons. To do that one can use the MLP network. Later single leptons are combined to like-sign and unlike-sign pairs in order to reconstruct signal pairs (see Chap. 5.3). First of all one should point out that after applying PT3 trigger conditions ($M_{TOF} \geq 20$) and fulfilling the condition of having at least one hit in the Start detector, $4.7 \cdot 10^9$ events are used for further analysis. For all investigations made in

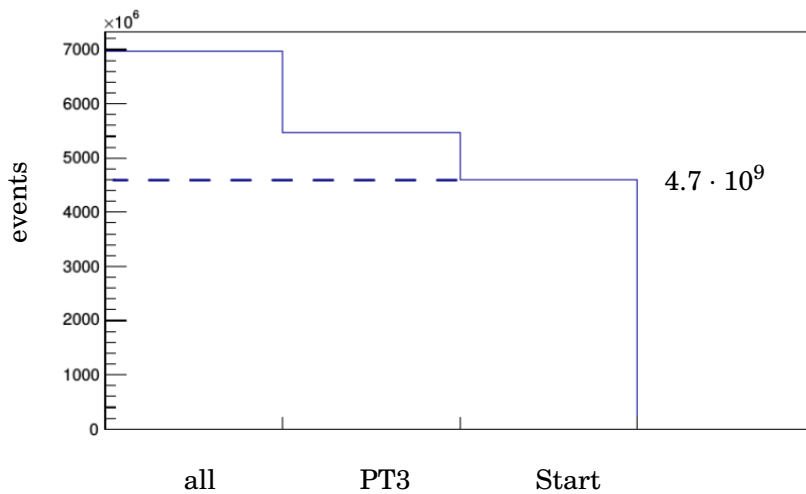


Figure 5.1: Total number of registered events in the Au+Au beamtime in 2012 after PT3 trigger and at least one registered hit in start or veto detector.

this chapter (analysis of single lepton candidates) the subset of three days of the whole beam time were used. Considering a particle velocity between 0.9 and 1.5, $1.91 \cdot 10^7$ particles were registered in the RPC region and $1.02 \cdot 10^7$ particles in the TOF region after track pre-selection and sorting. The pre-selection of the lepton track candidates is based on a set of criteria which help to distinguish them from the hadron track candidates. In the track sorting the possible track candidates are compared with each other and the “best” candidate, based on the pre-selection criteria, is chosen for the following analysis. For track candidates pre-selection the following criteria are required:

- track candidate was fit with Runge-Kutta fitter ($\chi^2 > 0$) and track is considered if

$$\chi^2 < 500,$$

- hit in every detector, including one hit in the RICH detector,
- velocity of the particle $\beta > 0.9$,
- $50 \text{ MeV}/c < \text{reconstructed momentum} < 1500 \text{ MeV}/c$.

The β versus momentum distribution in the RPC and TOF regions are shown in Fig. 5.2. One can clearly see the leptons settled around $\beta = 1$ and the π^+/π^- which are entering the distribution at a lower β . At around $350 \text{ MeV}/c$ electrons and pions start to overlap. In the following section (Sec. 5.1) we discuss, how the leptons could be identified by using the MLP network.

5.1 Use of the MLP Network for Electron Identification

In order to receive the response from the neural network one has to train it with a chosen input sample for background and signal. All particles with a richQa value $< 0.5^\circ$ are defined as a signal whereas particles with a richQa value $> 7^\circ$ are set as background (see Chap. 4.5). To get an input sample with enough statistic for training the neural network, statistic of 5 days was analysed. Each sample (input and background) has a size of around 10^6 stored particles for RPC and TOF region. In the training procedure signal and background is weighted equally. For the TOF region 8 variables are used to train the neural network, whereas 9 variables are used in the RPC region. All variables are listed in Tab. 5.1. One should use only variables which are not correlated with each other, otherwise one of the correlated variables gives no more benefits in identifying leptons. Each independent variable improves the output of the neural network. In Fig. 5.3 the correlation matrix is shown for background and signal in the RPC and TOF regions. For example the ring Hough Transform (ringHT) and number of fired pads per ring (ringNP) are correlated strongly with each other in the signal sample. In this case it was decided to keep both variables to train the neural network, because the same type of the correlation in the background sample is located around 47 %.

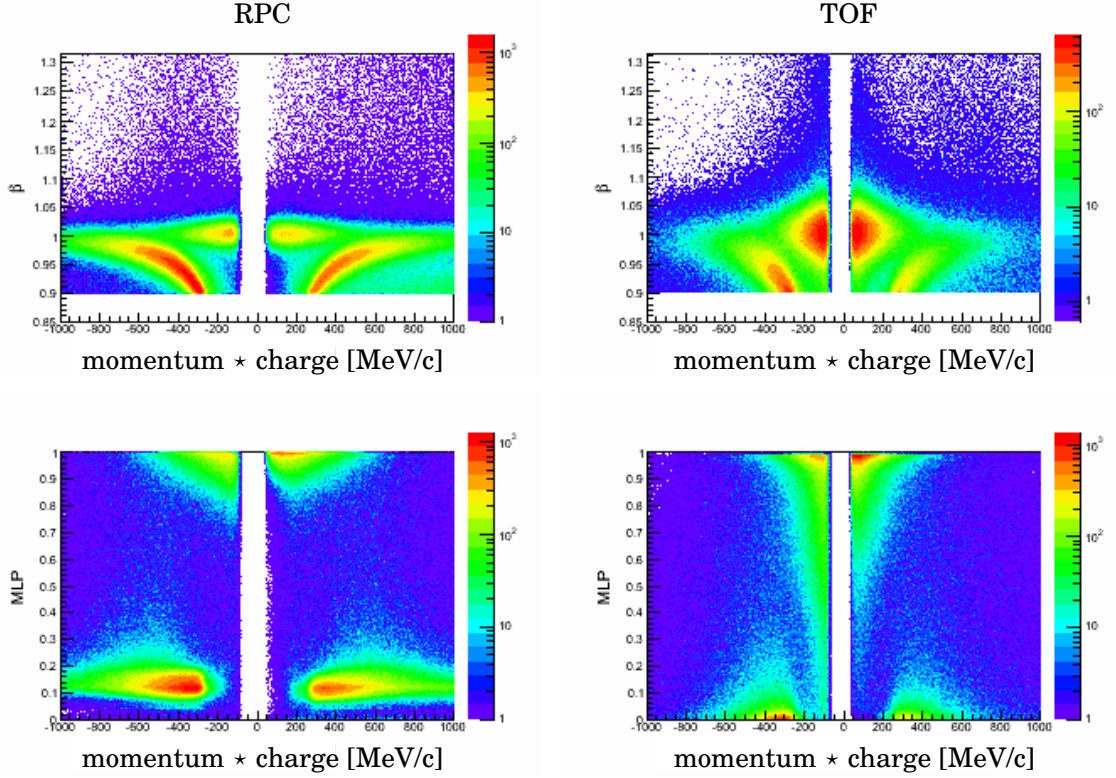


Figure 5.2: Upper row: β versus momentum for RPC (left) and TOF (right) region. Lower row: Response of the MLP network for RPC (left) and TOF (right) region.

short cut	description
ringNP	Number of fired ring pads in the RICH
ringAC	Average charge of a ring which is detected in the RICH
metaQa	Matching quality between tracking system and time-of-flight systems
ringHT	Hough Transform algorithm helps to identify objects (e.g. circles). It calculates the center of all possible rings and gives a value back. The height of the center maximum corresponds to a high HT quality.
beta	Velocity of a particle
richQa	Quality parameter of the matching of a ring to a reconstructed track
mdcdEdx	Specific energy loss in the MDC
theta	Polar angle of the reconstructed track
showerDq	Integrated charge which is deposited in the pre-shower detector (RPC region)
momentum	Reconstructed momentum of a particle (RPC region)
tofdEdx	Energy loss in the TOF detector (TOF region)

Table 5.1: Overview over all variables included for the training and testing of the neural network.

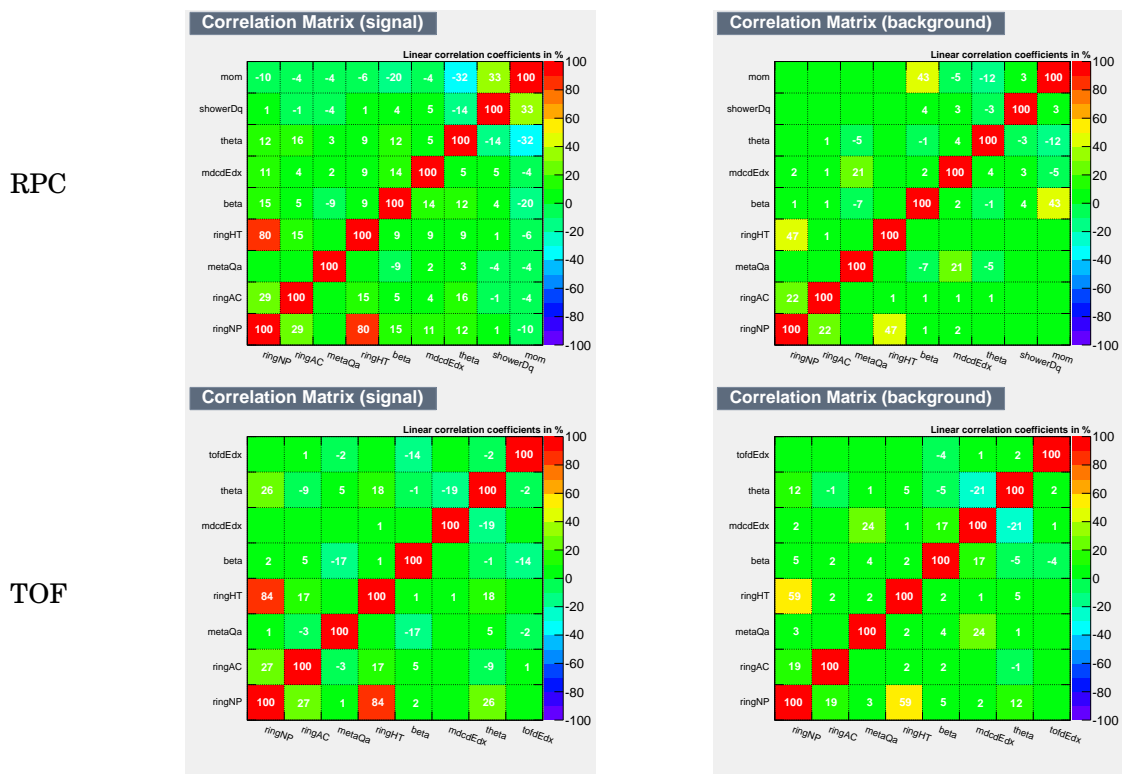


Figure 5.3: Upper row: Correlation matrix in the RPC region. The values are representing the correlation of two variables in percent. Lower row: Correlation matrix in the TOF region. Boxes without values have correlations close to 0.

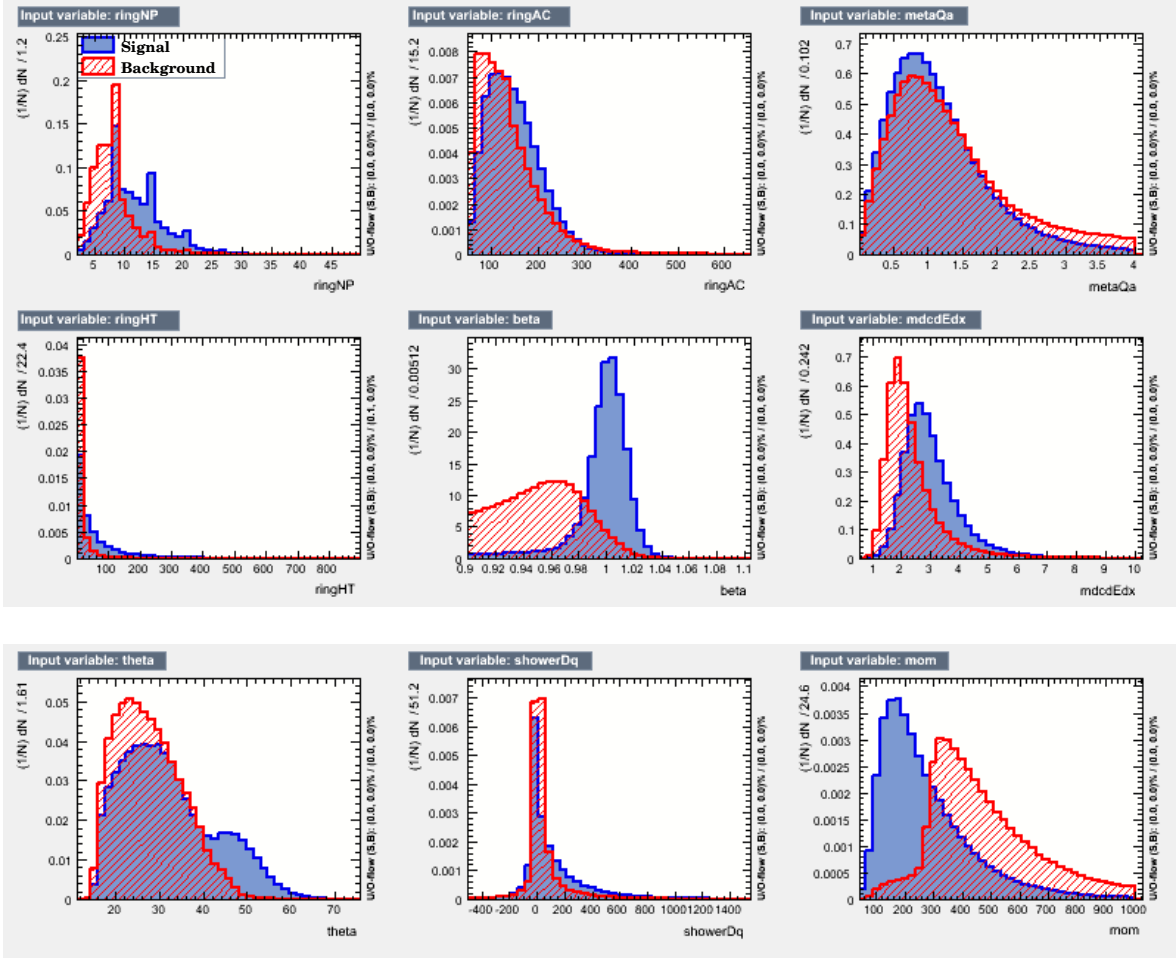


Figure 5.4: Signal and background distribution for each input variable separately in the RPC region.

To visualize how useful are the input variables to distinguish between leptons and hadrons the distribution of signal and background for each variable is plotted in Fig. 5.4 (in the RPC region) and 5.5 (in the TOF region). Variables for which one has a smaller overlap between background and signal (e.g. β , momentum) are more powerful to distinguish between leptons and hadrons than variables which have a large overlap between background and signal (e.g. metaQa). The β distribution for leptons looks like a gaussian distribution around $\beta=1$, whereas hadrons have a $\beta < 1$.

After training the neural network one gets a value between 0 and 1 as a response, called MLP response value. The distribution of the MLP response value versus momentum is plotted in Fig. 5.2. Leptons are settled around an MLP of 1 and hadrons are visible in the range of a lower MLP. Whereas leptons and hadrons are well separated from each other in the RPC region, in the TOF region leptons are entering regions with a lower MLP response in the low momentum range. Regarding the statistic in the region with momentum < 200 MeV/c and MLP < 0.6 it was chosen to neglect the leptons in this range in order not to contaminate the lepton sample with hadrons. In further analysis steps cuts on MLP > 0.6 and richQa $< 2^\circ$ are applied, these cuts provide the best efficiency and purity of lepton identification.

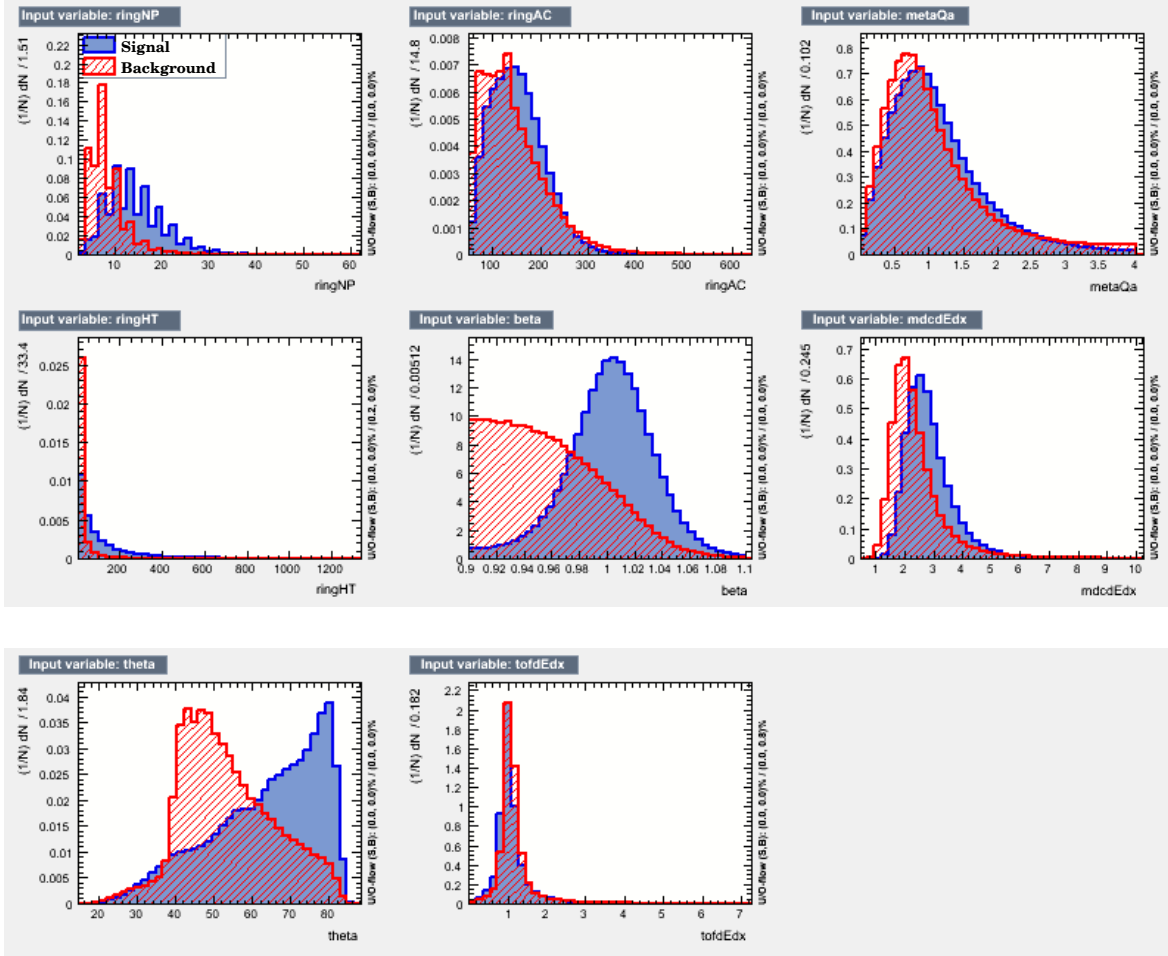


Figure 5.5: Signal and background distribution for each input variable separately in the TOF region.

To optimize the set of input variables, three different cases have been investigated.

- Including θ , charge in the Pre-Shower detector (showerDq) and momentum separated (case 0)
- Without θ , charge in the Pre-Shower detector (showerDq) divided by momentum (showerDq/momentum) (case 1)
- Without θ , charge in the Pre-Shower detector (showerDq) and momentum separated (case 2)

In order to analyse the effect, which the different set of input variables could have on the MLP response and therefore on the cut efficiency and purity of the lepton sample, one can monitor the β versus momentum distribution after applying cuts. The results are shown in Fig. 5.6.

To determine the purity of such lepton samples in the experimental data the “rotated RICH detector method” can be used, see Fig. 5.7. In this case the same analysis is applied to data in which the RICH detector is rotated software-wise by 60° . After matching reconstructed tracks to hits in the RICH detector wrong matched tracks are found. In Fig. 5.9 the ratio between the wrongly matched tracks from the “rotated RICH detector method” and the total amount of matched tracks (from standard data analysis) is plotted. With respect to the amount of

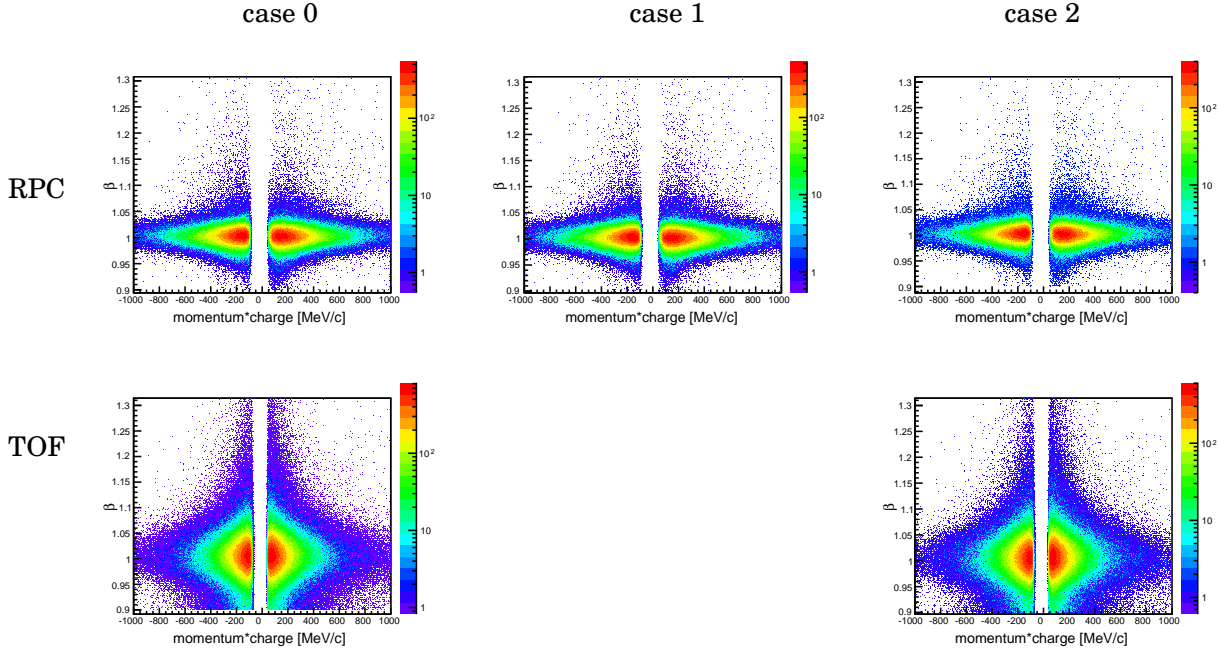


Figure 5.6: β versus momentum distribution after applying richQa $< 2^\circ$ and MLP > 0.6 . The shape of all five distributions looks the same. A cut on $\beta > 0.9$ is applied already on the pre-selection level.

background in the lepton sample after applying cuts one can conclude that case 0 and case 2 are providing the best results. In the lower momenta region ($p < 400$ MeV/c) a purity of $\sim 95\%$ is reached in the RPC region and approximately 90% in the TOF region. For the U boson search we concentrate mainly on the invariant masses $M_{ee} < 300$ MeV/c². This mass range is dominated by leptons. Fig. 5.8 shows the momentum distribution of leptons before identification cuts are applied (red curve) and after identification cuts based on MLP response for case 0, 1, 2. Above 350 MeV/c hadrons are clearly contaminating the distribution, if no lepton identification cut is applied. In addition one can clearly see the advantage of case 0 and case 2, since the efficiency and purity of both cases show better performance compared to case 1. Independently whether θ is included in the set of variables for the neural network training or not, the momentum distribution has the same statistics and shape. From this point of view it does not matter if the polar angle is used or not for training purpose. To validate further different analysis strategies they have been checked towards simulated data and the results are discussed in Sec. 5.1.1.

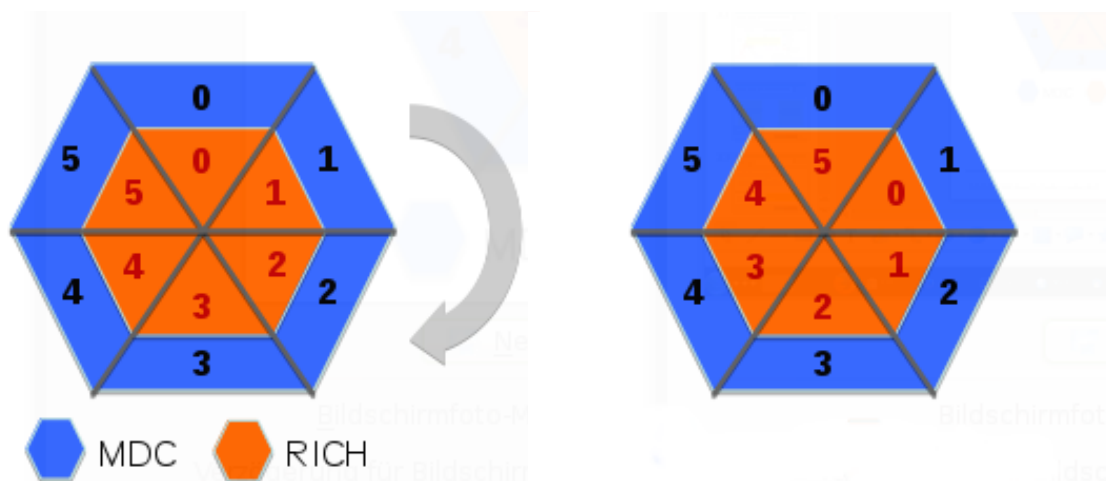


Figure 5.7: The HADES spectrometer is built up of six sectors. In the “rotated RICH detector method” the RICH detector is rotated software-wise by 60° . After rotation the MDC sector and the RICH sector is shifted by one sector clockwise.

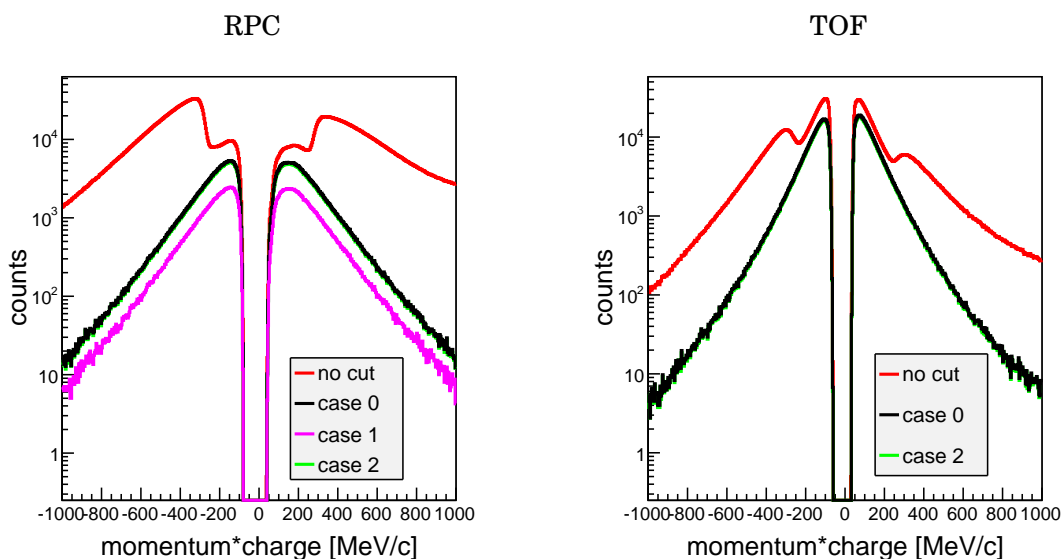


Figure 5.8: Momentum distribution without ID cut (red curve) and for different cases. The distributions without ID cut are contaminated by hadrons at $p > 200$ MeV/c. Case 0 and 2 coincide, whereas case 1 has less leptons left after applying both cuts ($\text{richQa} < 2^\circ$ & $\text{MLP} > 0.6$) to the three different cases.

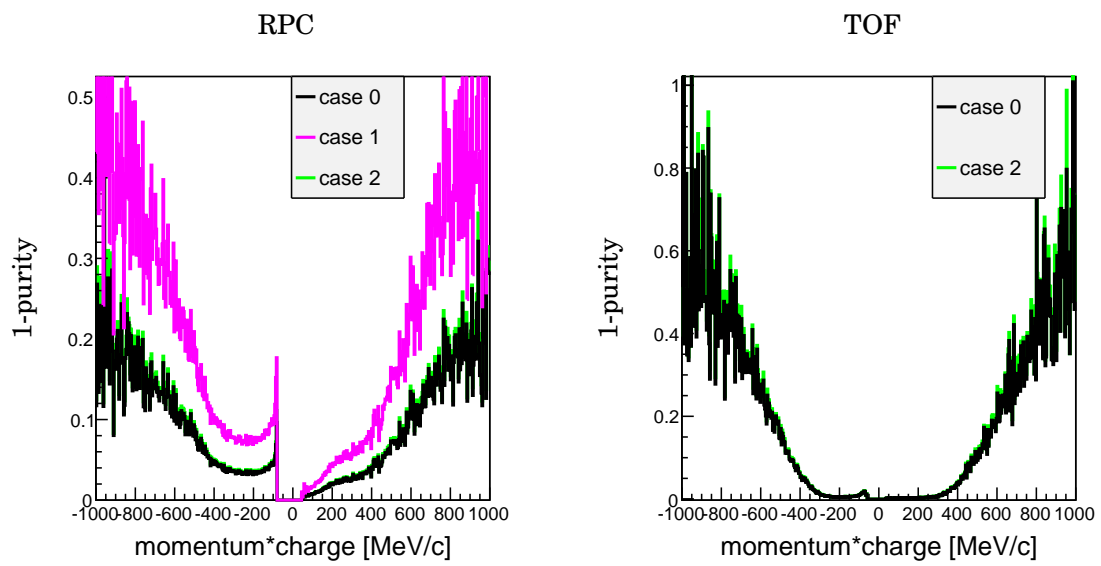


Figure 5.9: Percentage values of background in the lepton sample as a function of momentum in experimental data. Case 1, in which no θ is included and where deposited charge in the shower detector is divided by the momentum, shows the worst percentage values. The amount of wrongly matched tracks is higher than in case 0 and 2. For case 0 (with θ and case 2 (no θ) the amount of background is in the same order.

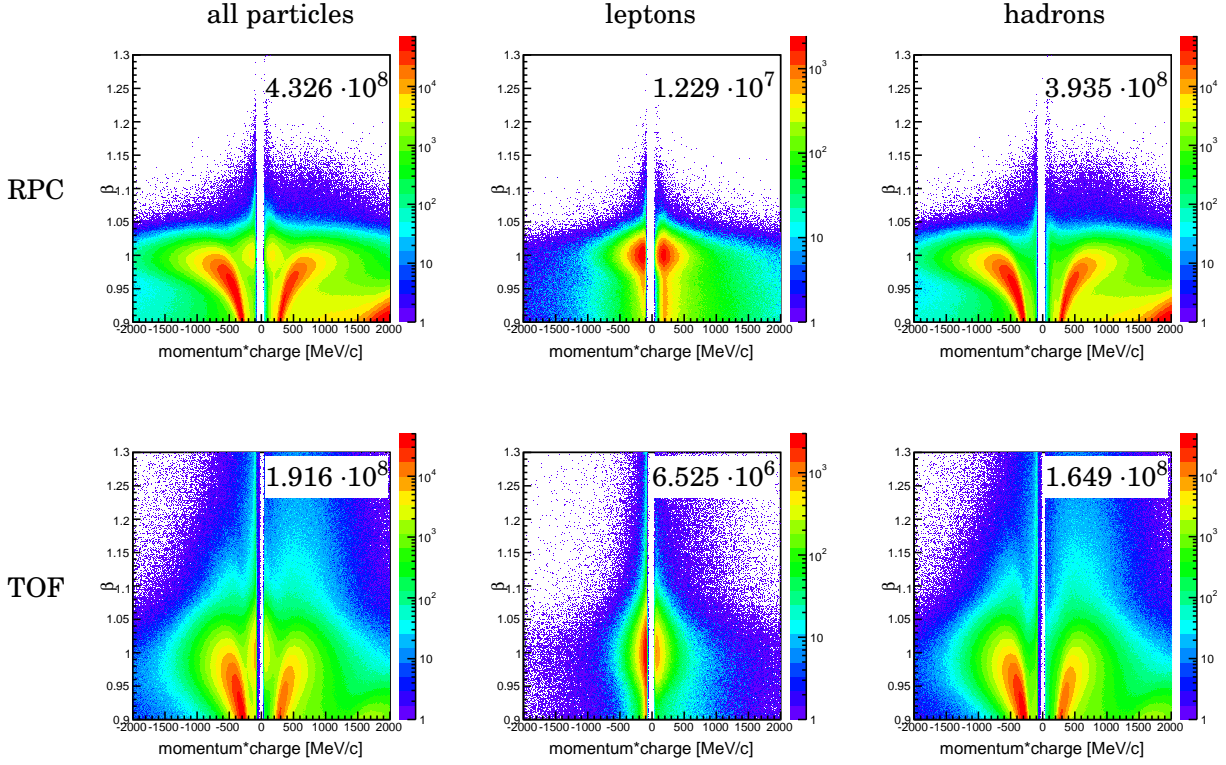


Figure 5.10: β versus momentum distribution for RPC and TOF region without any particle identification cut. The integral of the distribution is shown in the top right corner. **Left column:** Without asking for the GeantPID number (all particles). **Middle column:** Asking for GeantPID of leptons. **Right column:** Asking for GeantPID of hadrons.

5.1.1 Validations with Simulation Data

The simulation is produced to be as close as possible to the real measurement (see Sec. 5.3.2). The same analysis is performed on the simulation data as on the real data. One benefits of the simulation since it holds more information as the real data. One can access the information about each particle during the whole analysis process. Later the information can be used to compare it with the parameters which one gets out of the analysis of the real data. In the following chapter the particle identification information “geantPID” is used to distinguish between leptons and hadrons in order to determine purity and efficiency of a particle sample.

- Geant PID: 2 (e^+), 3 (e^-)
- Geant PID 8 (π^+), 9 (π^-), 14 (proton)

Purity is defined as

$$\text{purity}_{\text{lep}} = \frac{\text{lep}_{\text{after cut}}}{\text{all particles}_{\text{after cut}}}, \quad \text{purity}_{\text{had}} = \frac{\text{had}_{\text{after cut}}}{\text{all particles}_{\text{after cut}}}. \quad (5.1)$$

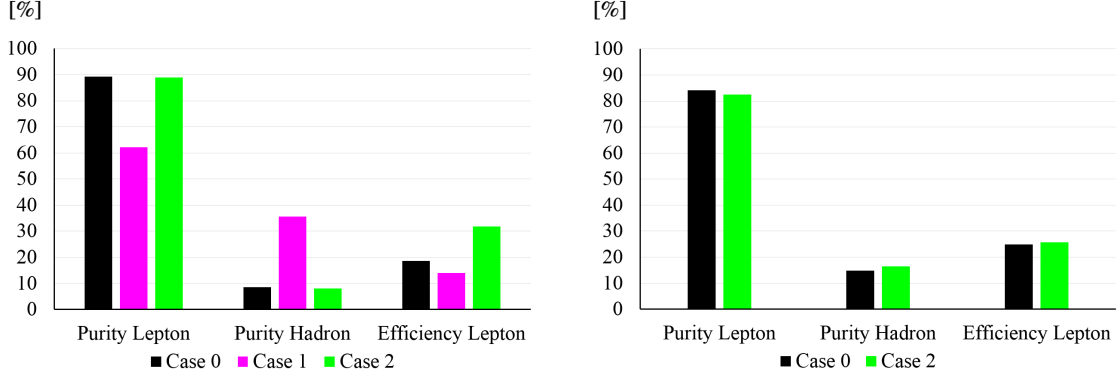


Figure 5.11: Percentage values of purity and efficiency in the TOF (right panel) and RPC (left panel) regions. Efficiency for hadrons is of the order of 10^{-3} to 10^{-4} and can not be displayed in the same chart. A particle identification cut of $MLP > 0.6$ is applied.

whereas efficiency is defined as

$$\text{efficiency}_{\text{lep}} = \frac{\text{lep}_{\text{after cut}}}{\text{lep}_{\text{before cut}}}, \quad \text{efficiency}_{\text{had}} = \frac{\text{had}_{\text{after cut}}}{\text{had}_{\text{before cut}}}. \quad (5.2)$$

For the analysis 10^7 simulated events are used in order to get enough statistic. The β versus momentum distribution is displayed in Fig. 5.10 (top panel) without any particle identification cuts. The hadrons, especially π^+ and π^- , start to contaminate the lepton distribution above momentum of 300 MeV/c. Whereas hadrons (π^+/π^-) have lower β , it gets close to $\beta = 1$ above momentum of 500 MeV/c. Protons are reaching β above 0.9 not before they have momentum of 1500 MeV/c in the RPC region. The β versus momentum distribution for different particles in the TOF detector is shown in Fig. 5.10 (bottom panel).

If one sets the condition that a particle should have an MLP response larger than 0.6 only $\sim 9\%$ of the hadrons are left. The calculated purities and efficiencies are visualized in Fig. 5.11 after an MLP cut and in Fig. 5.12 after MLP and richQa cuts.

Regarding the percentage values after the cut on the MLP response the training with the variable “showerDq” divided by the momentum gives the result with the worst numbers. About 35% of hadrons are left, whereas a lot of leptons are cut out. The situation is better after training the neural network with the variables “showerDq” and momentum separated from each other. The only difference in the input variables is the angle θ , which is included in case 0. After the MLP cut both sets of variables are delivering almost the same numbers for efficiency and purity.

In order to reach a higher lepton purity the richQa cut smaller than 2° is applied. Whereas around 20 % of leptons surviving the MLP cut only around 13% of all leptons are entering the distribution after MLP and richQa cut. But one gains 9 % (case 0) in lepton purity. The resulting velocity versus momentum distributions are shown in Fig. 5.13 after the $MLP > 0.6$ cut is applied and in Fig. 5.14 after an additional cut on ring-to-track matching quality cut ($\text{richQa} < 2^\circ$) is applied.

Regarding the lepton purity and efficiency values the case 0 is the best choice. Analysing the simulation data confirms the results which one gets from the experimental data. The polar angle θ should be kept as an input variable for training the neural network.

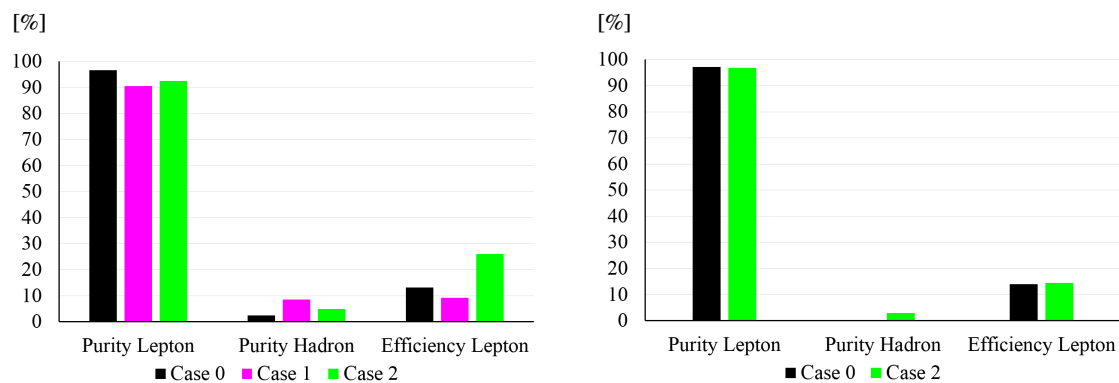


Figure 5.12: Percentage values of purity and efficiency in the TOF (right panel) and RPC (left panel) region. Efficiency for hadrons is of the order of 10^{-3} to 10^{-4} and can not be displayed in the same chart. Particle identification cuts of $MLP > 0.6$ and $richQa < 2^\circ$ are applied.

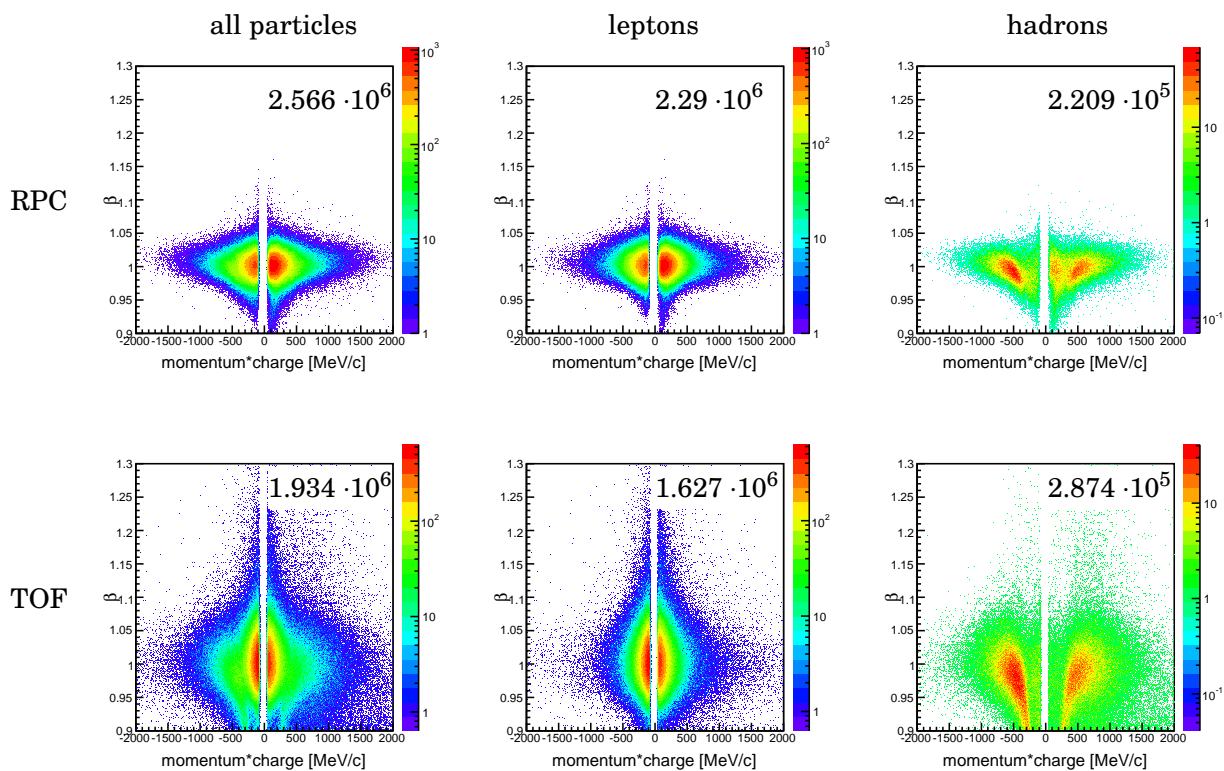


Figure 5.13: β versus momentum distribution for RPC and TOF region after a particle identification cut $MLP > 0.6$. The integrals of the distribution are shown in the top right corners.

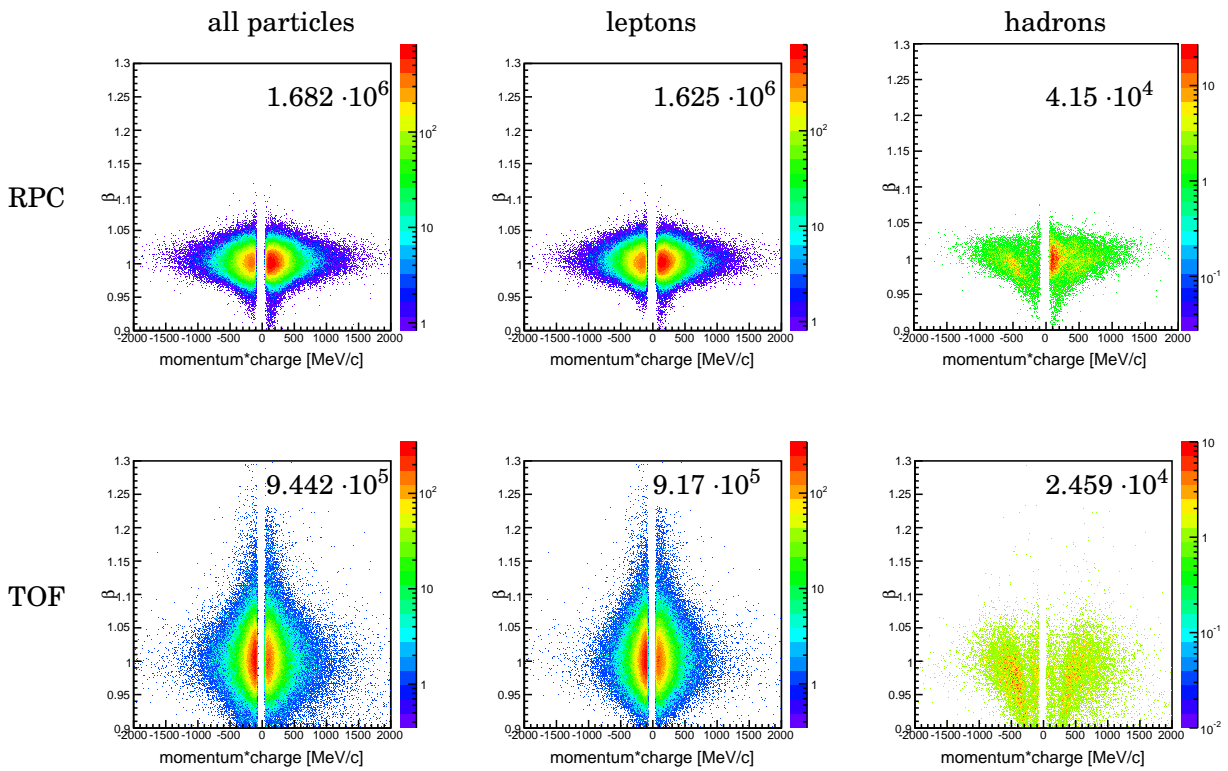


Figure 5.14: β versus momentum distribution in the RPC and TOF regions after particle identification cuts $MLP > 0.6$ & $richQa < 2^\circ$. The integrals of the distribution are shown in the top right corners.

5.2 Correction of META dx in the TOF region

For identification of leptons the ring matching quality is used. The so-called richQa value is described in chapter 4.5. In a similar way a matching quality between the reconstructed track and the META detector is defined. The metaQa value is defined as

$$\text{metaQa} = \sqrt{\frac{dx^2}{\delta dx^2} + \frac{dy^2}{\delta dy^2}} \quad (5.3)$$

where dx and dy are the differences between the projection of the reconstructed track in the drift chambers and the hit position measured in the META detector, and δdx and δdy are the associated uncertainties. A metaQa is needed for the quality of the reconstructed tracks. For lepton selection a metaQa value smaller than 4 is used as a cut value. In Fig. 5.15 the polar

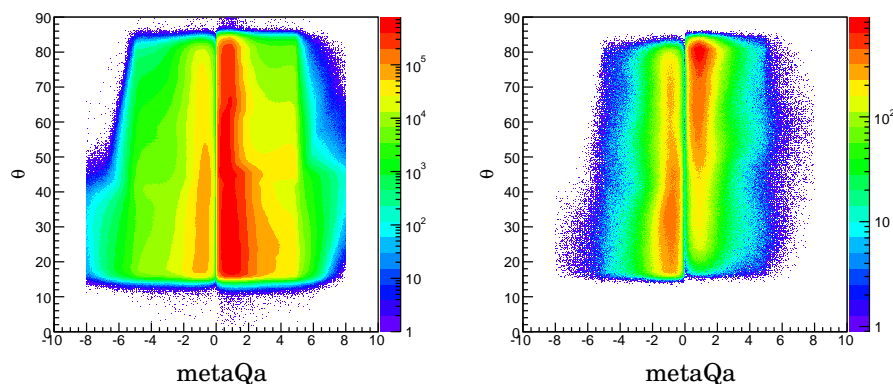


Figure 5.15: Polar angle θ as a function of the the metaQa*polarity value. **Left column:** Without any cut and plotted for all particles. **Right column:** Same distribution but after applying lepton identification cuts: RichQa < 2, effective mass < 90 MeV/c².

angle θ as a function of the metaQa value is shown for positive and negative particles. Looking closer to each part of the metaQa variable separately, namely to the META dx distribution, systematics, like oscillations in the mean value of the dx distribution, are getting visible. A detailed study of the dx variable in the TOF detector was performed in order to understand better the observations. The obtained mean and RMS of the dx distribution for each TOF cell is shown in the Fig. 5.16 (upper panel). In comparison to the dx distribution obtained from simulation (see Fig. 5.16 - lower panel) the mean value is oscillating around 0 with a maximum of 4 and minimum of -4 for pions in a momentum range of 500 - 600 MeV/c. In order to apply later efficiency corrections the simulation and the experimental data must agree. So the aim is to correct META dx in the TOF detector in order to get the mean value to 0 for all sort of particles.

Therefore a META dx versus β distribution is plotted for each cell individually. META dx versus β is shown for one cell as an example in Fig. 5.17 (left column). Splitting now the velocity axis in 20 slices and projecting dx to it, the mean and RMS value can be extracted directly out of the distribution as shown in Fig. 5.17 (right column). The mean value has a growing trend with β , therefore in order to correct META dx for every particle type the correction has to be β dependent.

The mean and RMS is now stored for each cell β dependent to a parameter file, which can be read by everyone who needs a META dx correction. After applying the correction the mean of

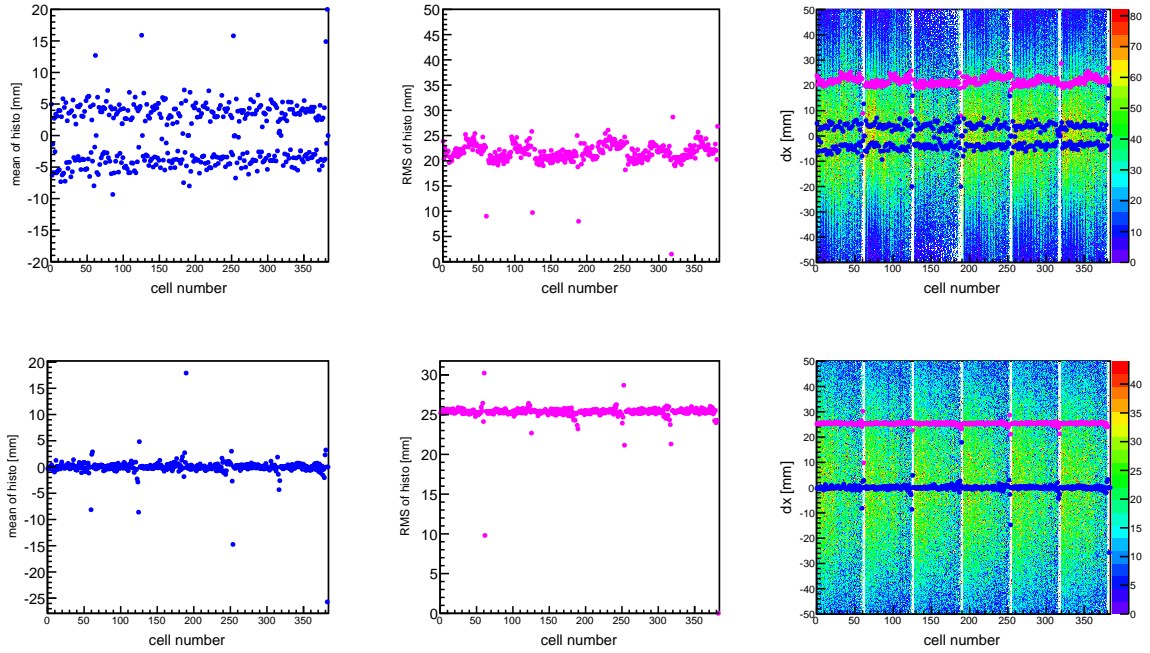


Figure 5.16: **Upper panel:** Characterization of the dx distribution for all the scintillator cells for negative pions with a momentum between 500-600 MeV/c. In the left are plotted the residuals, in the center the RMS and in the right panel the scattered plot with the first panels together. **Lower panel:** Same as upper but for simulated data.

the dx distribution is consistent with simulation, see Fig. 5.18. We can investigate the effect of the corrected dx value. First we recalculate the variable $metaQa$, by using the corrected dx value and error (derived from the gaussian distribution). If one looks at the statistical distributions of both coordinates, it is preferably to split the x - and the y - coordinate and to calculate the $metaQa$ only by using dx ; whereas y reflects the geometry of the META detectors as a square box, the x - coordinate follows a Gaussian distribution. The $metaQa'$ value is calculated as

$$metaQa' = \left| \frac{dx}{\sigma(dx)} \right|. \quad (5.4)$$

This new quality parameter ($metaQa'$) can be compared to the former defined $metaQa$. The effect of cutting on this recalculated observable from 4 to 1 is shown in Fig. 5.19 for θ and rapidity distribution. Notice that after correcting systematics and splitting to x and y coordinates separately the expected decrease in statistics by cutting on $metaQa$ is well reproduced. As the y coordinate in META is obtained from cell geometry, the tracks pointing outside a given cell were removed from the sample. In the left column in Fig. 5.19 θ and rapidity distribution is shown for different $metaQa$ cut values. Clearly visible is the loss of yield which is created by applying a stricter standard $metaQa$ cut (< 2). $metaQa$ is here calculated like in Eq. 5.3. Recalculating now $metaQa$ on the analysis level by using Eq. 5.4 and applying it to the rapidity and θ distribution the structure softens. For identifying leptons it plays no role because in this case only a cut $metaQa < 4$ is applied, but regarding particle identification of Kaons the recalculated META matching quality can be useful.

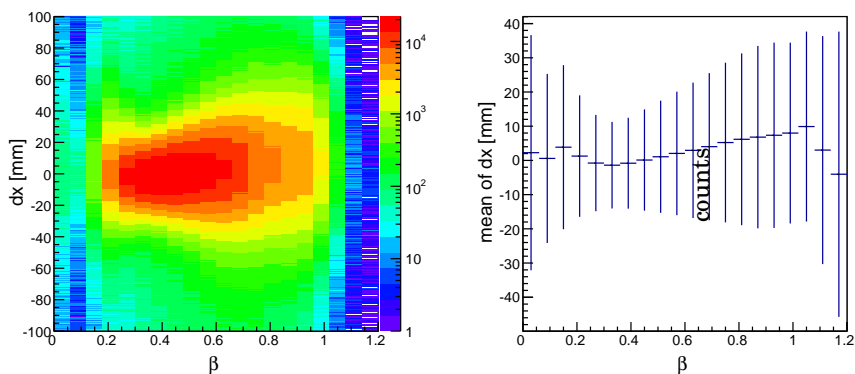


Figure 5.17: **Left column:** META dx versus β distribution for one cell of the TOF detector. **Right column:** Mean of the gaussian dx distribution calculated for one cell dependent on β , error bars are the gaussian sigma of the distribution.

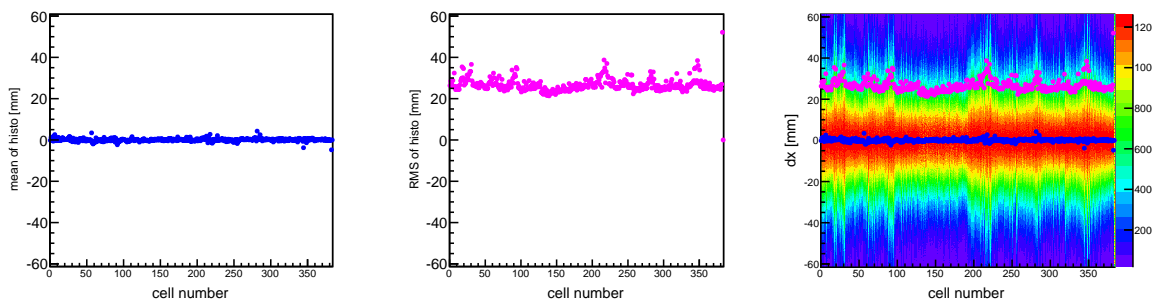


Figure 5.18: **Left column:** dx mean value obtained from the 2D distribution (right column). **Middle column:** RMS value calculated from the 2D distribution. **Right column:** Corrected META dx versus cell number distribution plotted for the TOF detector together with mean and RMS.

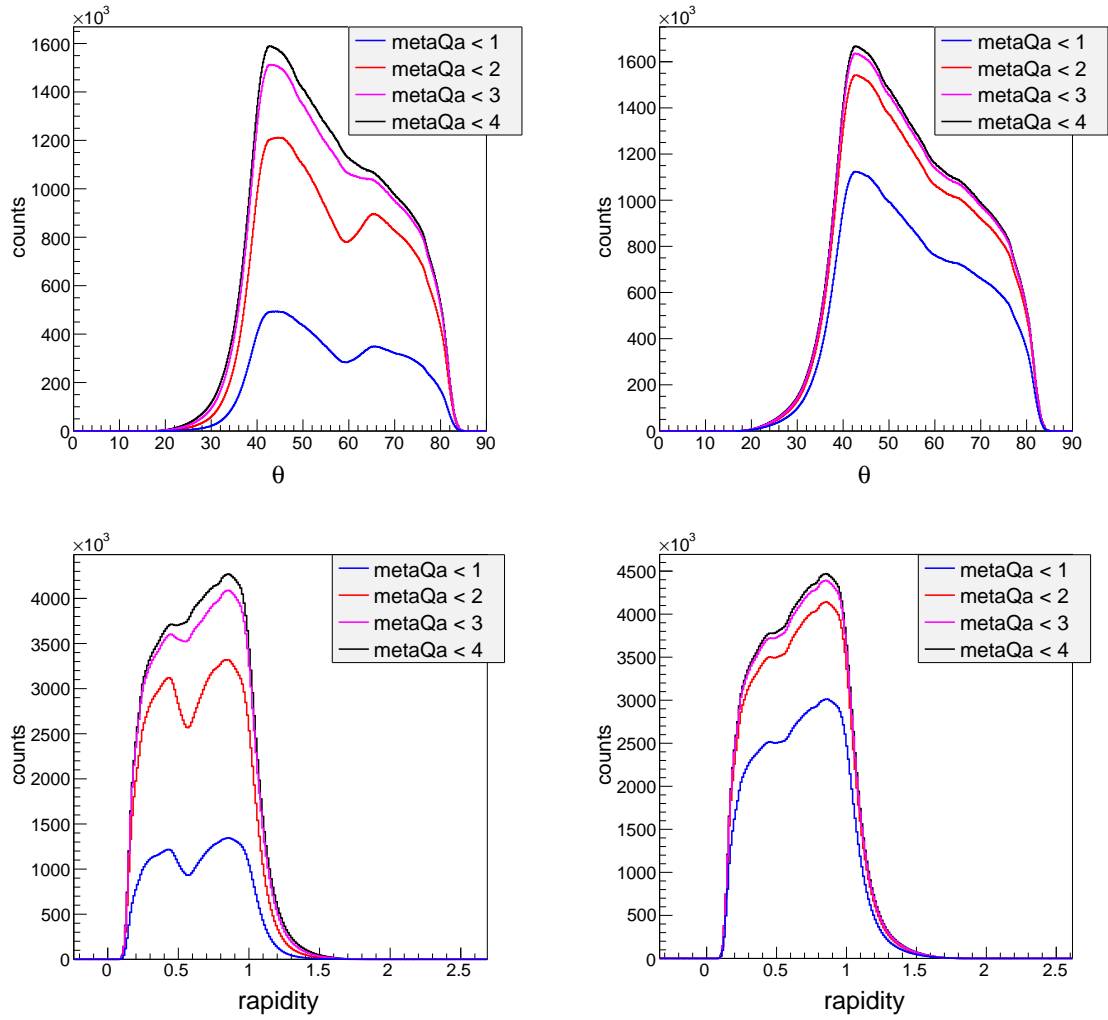


Figure 5.19: **Upper panel:** θ distribution for cuts on $\text{metaQa} = \sqrt{\frac{dx}{\delta dx}^2 + \frac{dy}{\delta dy}^2}$ (left column) and cuts on the new $\text{metaQa}' = \left| \frac{dx}{\sigma(dx)} \right|$ (right column). **Lower panel:** Same analysis applied to the rapidity distribution.

5.3 Inclusive Dilepton Spectrum

Dileptons are appropriate to investigate meson properties, like mass and decay width at extreme densities and temperatures, or to make investigations concerning chiral symmetry restoration, due to the fact that leptons do not interact via the strong interaction. They can escape from the point of reaction without losing any information about the reaction. The aim is to find truly correlated lepton pairs, originating from the same decay vertex.

The invariant mass of a lepton pair is given by

$$M_{e^+e^-}c^2 = \sqrt{(E_{e^+} + E_{e^-})^2 - (\vec{p}_{e^+}c + \vec{p}_{e^-}c)^2}, \quad (5.5)$$

where E_{e^+} , E_{e^-} are the total energies, \vec{p}_{e^+} , \vec{p}_{e^-} the momentum of the single lepton in laboratory system and c the velocity of light. For leptons with energies $E_{e^\pm} \cong 0.511 \text{ MeV}/c^2$ the equation 5.5 can be rewritten as

$$M_{e^+e^-} = \sqrt{2 \cdot p_{e^+}p_{e^-}(1 - \cos\theta_{e^+e^-})} = 2 \cdot \sin(\theta_{e^+e^-}/2) \cdot \sqrt{p_{e^+}p_{e^-}} \quad (5.6)$$

with $\theta_{e^+e^-}$ is the opening angle between the two lepton tracks.

One has to deal in HADES with two dominant sources of lepton pairs:

- external photon conversion in the target, RICH radiator and RICH carbon shell - pair creation $\pi^0 \rightarrow \gamma (\gamma \rightarrow e^+e^-)$,
- dalitz decay of the π^0 meson - $\pi^0 \rightarrow \gamma e^+e^-$.

At higher masses the pairs are mostly coming from:

- η Dalitz ($\eta \rightarrow \gamma e^+e^-$) decays,
- Δ Dalitz, N^* Dalitz, ω Dalitz $\rightarrow \gamma e^+e^-$ ($\Delta \rightarrow Ne^+e^-$, $N^* \rightarrow Ne^+e^-$, $\omega \rightarrow \pi^0 e^+e^-$),
- pn Bremsstrahlung,
- direct decays of ρ , ω and $\phi \rightarrow e^+e^-$.

The main characteristic of the e^+e^- pairs originating the external γ conversion is small opening angle, below few degrees (3°). Fig. 5.20 (left) shows opening angle distribution for various lepton sources. In the following analysis minimum cut of 9° has been applied, which is removing mostly pairs coming from γ . This cut removes partially contribution from π^0 and η Dalitz decays, but the situation with the signal-to-background is removed.

5.3.1 Calculation of the Combinatorial Background

From all reconstructed single leptons tracks which passed MLP cut, pairs with all possible combinations are built up in each event. They are combined into a like-sign ($N_{e^+e^+}$, $N_{e^-e^-}$) and an unlike-sign pair ($N_{e^+e^-}$). Fig. 5.21 (left) shows invariant mass distributions of such like-sign and unlike-sign pairs. The dilepton spectrum consists of the true pairs, which is of our interest, and uncorrelated pairs, which are belonging to the combinatorial background.

The lepton pairs can be classified in two categories:

- correlated pairs, coming from true leptons and positron source,
- combinatorial pairs, built up from lepton and positron from different sources.

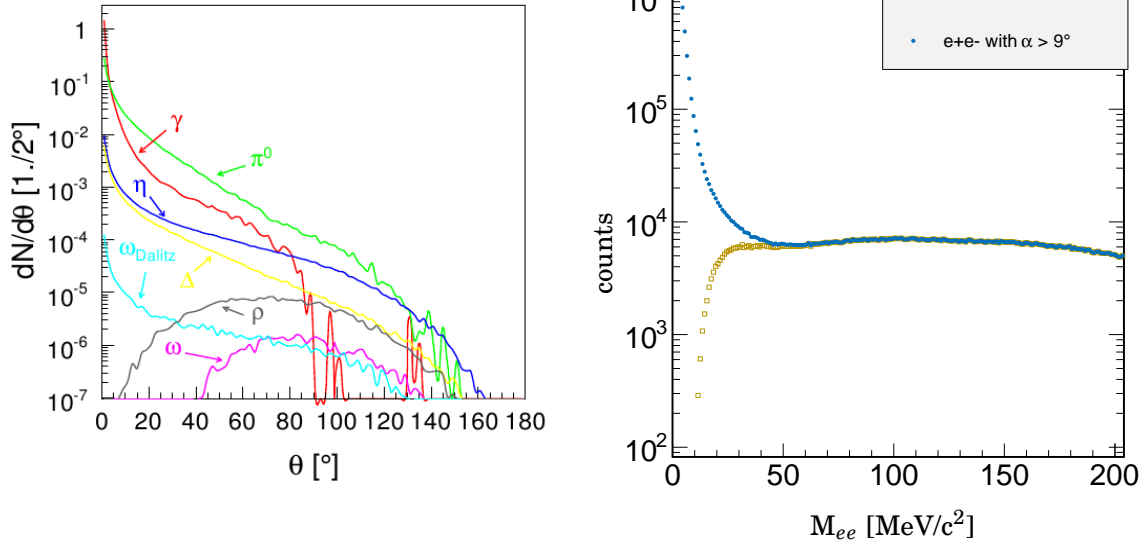


Figure 5.20: **Left:** Opening angle distribution for different lepton pair sources [27]. **Right:** Comparison between the unlike-sign lepton pair distribution with and without opening angle cut ($\alpha < 9^\circ$).

In order to extract from data pairs which corresponds to signal ($S_{e^+e^-}$), from the total $N_{e^+e^-}$ spectra combinatorial background ($CB_{e^+e^-}$) has to be subtracted.

$$CB_{e^+e^-} = 2 \cdot \sqrt{N_{e^+e^+} \cdot N_{e^-e^-}} \quad (5.7)$$

$$S_{e^+e^-} = N_{e^+e^-} - CB_{e^+e^-} \quad (5.8)$$

The $S_{e^+e^-}$, $CB_{e^+e^-}$ and $N_{e^+e^-}$ distributions with an opening angle cut of 9° is shown in Fig. 5.21 (right). The combinatorial background is estimated using geometry of same-event like-sign pairs.

5.3.2 Efficiency Corrections

To get the total yield of dileptons in the HADES acceptance, the measured like- and unlike-sign spectra have to be corrected by an efficiency factor. This factor reflects the probability smaller than 100 %, that the particle will be detected and reconstructed in the spectrometer, as well as inefficiencies of lepton identification cuts. The efficiency correction is calculated for single leptons separately and afterwards the product of two weights is gives the correction for pair, for example for an unlike-sign pair:

$$\text{weight}_{\text{pair}} = \text{weight}_{e^+} \cdot \text{weight}_{e^-} = \frac{1}{\text{efficiency}_{e^+}} + \frac{1}{\text{efficiency}_{e^-}} \quad (5.9)$$

and analogous for like-sign pairs. The efficiency correction for single tracks is calculated as a function of their phase-space parameters, θ , ϕ and momentum p . Therefore the weight used when adding an entry to any of the pair spectra is a function of 6 independent parameters - exactly the number necessary to fully describe the pair kinematics.

The single track efficiency is calculated by using the track embedding technique. Single electrons (and, separately, positrons) with uniform momentum p , ϕ and θ distributions are simulated using the Pluto event generator. The response of the detection system on them is simulated in GEANT and signals from the read-out of the detectors is emulated by digitizers built-in

to the Hydra framework. Such simulated track is then merged with measured experimental data (one simulated track per HADES sector in each of data events taken for this purpose). Then the full event is analyzed as usual in case of experimental data. The ratio of the number of embedded tracks that were reconstructed and went through all the identification cuts to those, which crossed the geometrical acceptance of the spectrometer (in a particular bin of p , θ and ϕ), is the reconstruction and identification efficiency.

For positrons it is shown in Fig. 5.23 as a function of momentum p and θ for different sectors (the ϕ dependence in each single sector is averaged-out). For θ angles below 60° it ranges between 20 and 45 % and for higher angles it is of the order of 60 %. The corrected and uncorrected spectra of all unlike-sign pairs and ratio of the two are shown in Fig. 5.22 (left panel). The effect of the efficiency correction is shown in Fig. 5.22 (right panel). The efficiency correction is largest for low mass region $M_{ee} < 150 \text{ MeV}/c^2$ and it is approximately factor of 5 for the $M_{ee} > 250 \text{ MeV}/c^2$

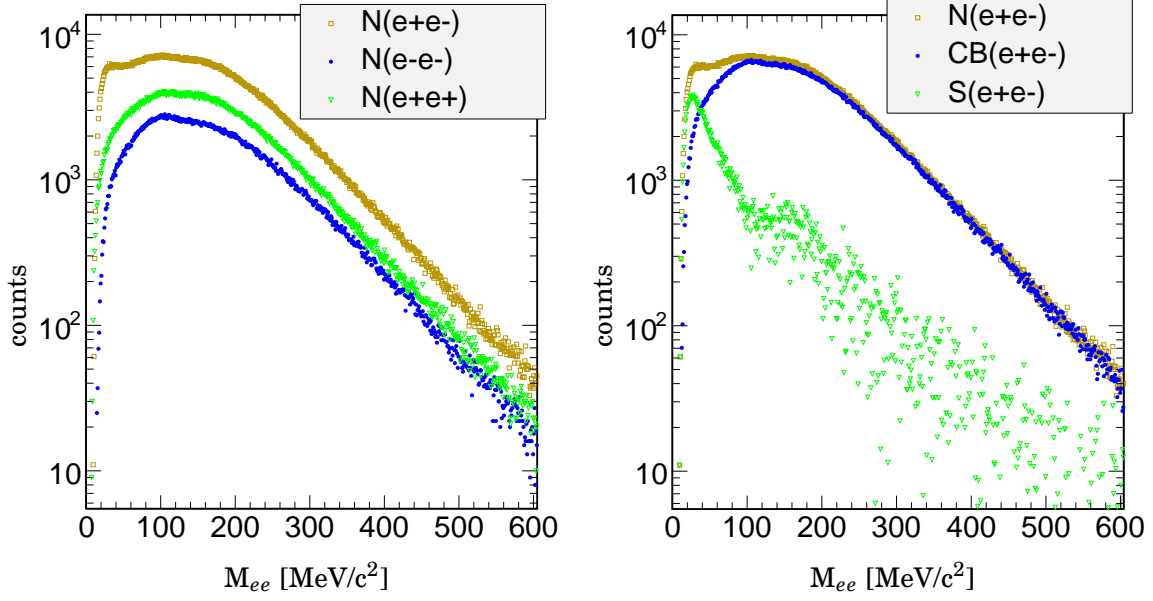


Figure 5.21: **Left:** $N_{e^+e^-}$, $N_{e^+e^+}$ and $N_{e^-e^-}$ distributions with an opening angle cut of $\alpha < 9^\circ$. **Right:** $N_{e^+e^-}$ (yellow squares) distribution together with the combinatorial background $CB_{e^+e^-}$ (blue circles) and the signal distribution $S_{e^+e^-}$ (green triangle).

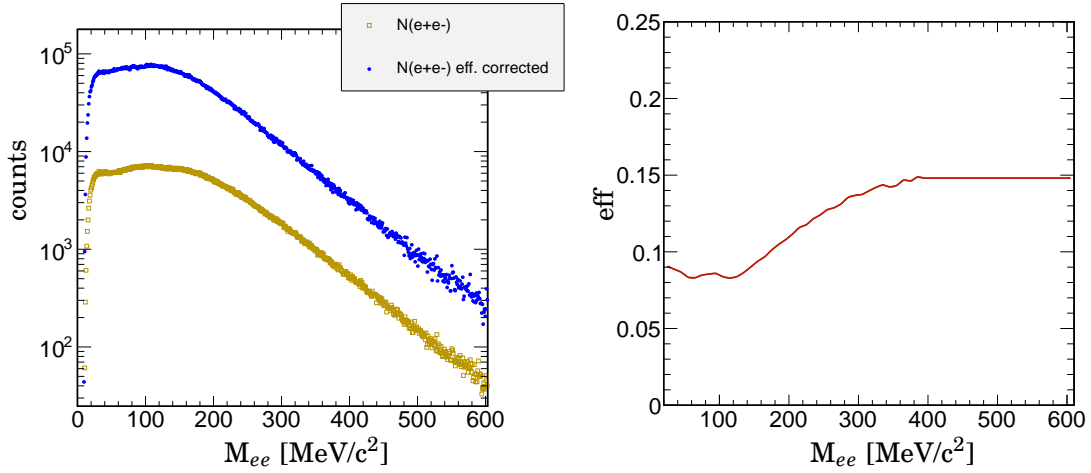


Figure 5.22: **Left:** Uncorrected (yellow squares) and corrected (blue circles) unlike-sign dilepton spectrum with an opening angle cut of 9° . **Right:** Efficiency correction factor as a function of invariant mass.

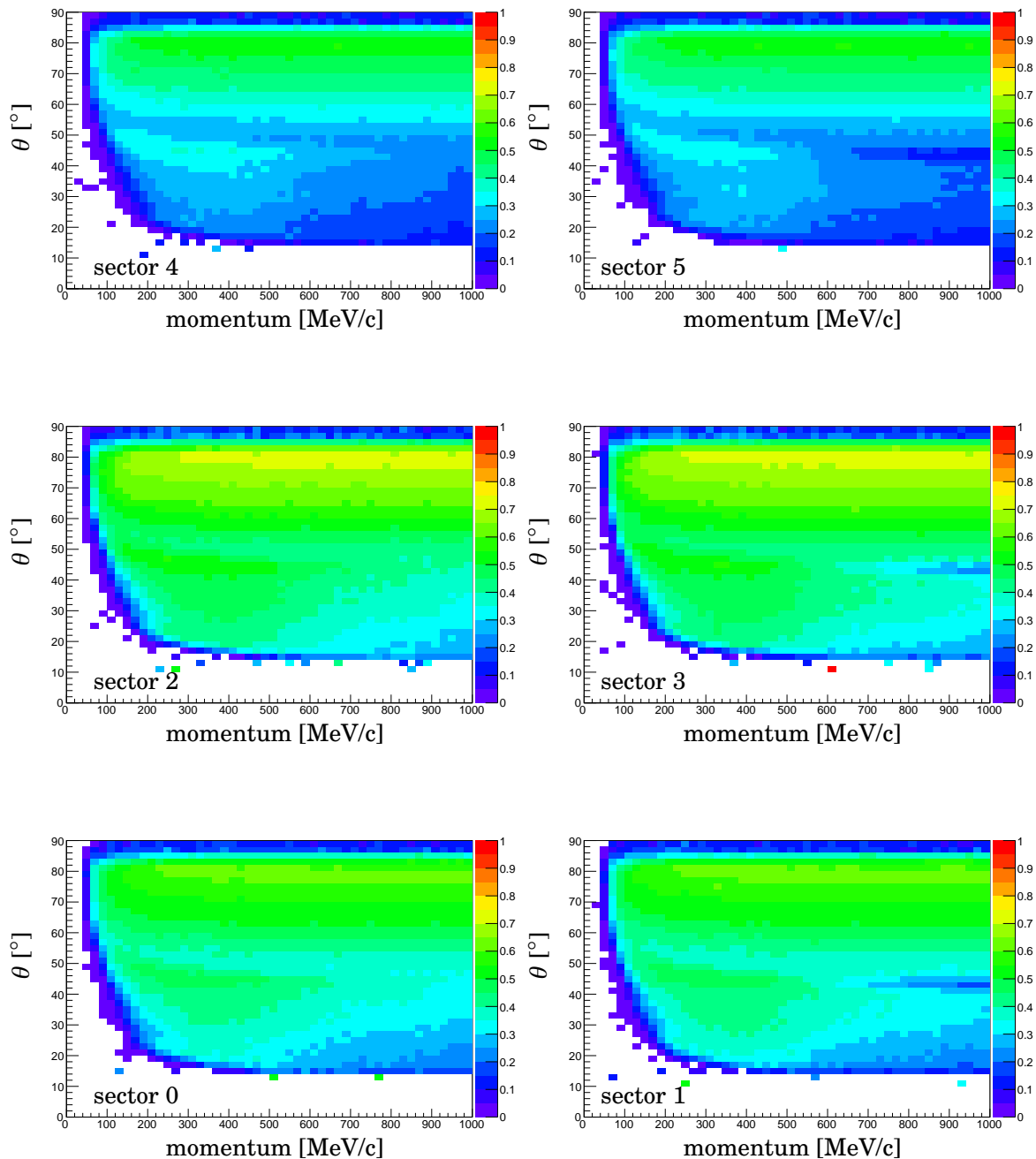


Figure 5.23: Positron reconstruction efficiency as a function of θ and momentum, averaged over all ϕ 's for every sector separately.

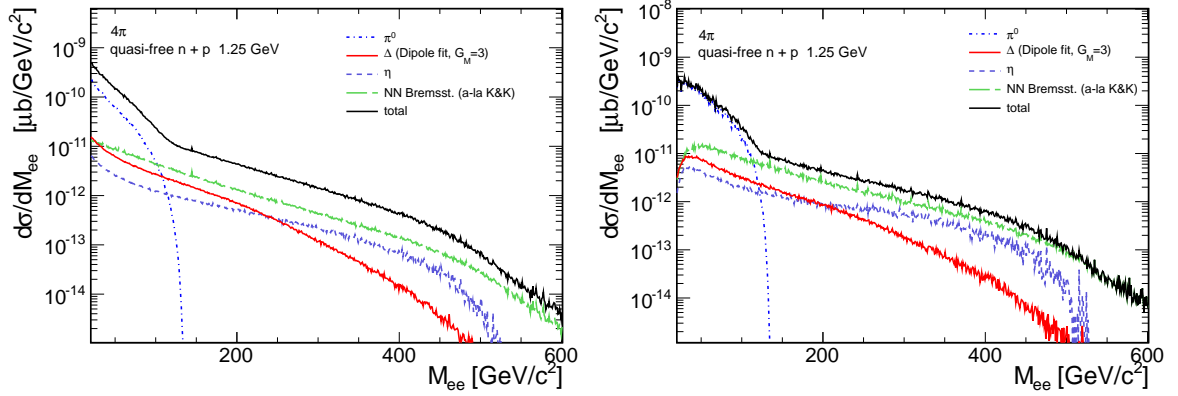


Figure 5.24: **Left:** Cocktail simulated with event generator Pluto [53] in full phase space. **Right:** Pluto cocktail inside HADES acceptance and with 9° opening angle cut.

5.3.3 Acceptance Corrections

Geometrical acceptance can be defined as a probability that a particle out of the reaction crosses the active volume of the HADES spectrometer. In order to build acceptance matrices the Monte Carlo method based on HGEANT has been used. Tracks with an uniform distribution in p , ϕ and θ are generated and tracked through the spectrometer assuming 100% detector efficiency. The accepted tracks are compared with the original ones and divided by each other. As a result one gets an acceptance matrix depending on p , ϕ and θ . The geometrical acceptance can be defined as:

$$Acc(p, \theta, \phi) = \frac{N_{acc}^{p, \theta, \phi}}{N_{tot}^{p, \theta, \phi}} \quad (5.10)$$

where $N_{tot}^{p, \theta, \phi}$ is the total number of tracks and $N_{acc}^{p, \theta, \phi}$ the tracks detected in the HADES spectrometer. The matrices of the acceptance depending on θ and p for positrons and electrons is shown in Fig. 5.25. The distributions are rather flat, however one can see the drop at low momenta (below 100 MeV/c). As expected the acceptance is going down for θ angles smaller than 18° and larger than 85° .

For our search of dark photon, acceptance as a function of invariant mass is needed. For this propose we used simulated cocktail for n+p (1.25 GeV) reactions with contributions from π^0 , Δ , η decays and Bremsstrahlung. Cocktail in full phase space and inside HADES acceptance with 9 degree opening angle cut are plotted in Fig. 5.24. Ratio of both distributions is later used as 1D acceptance correction for the dark photon search.

The unlike-sign pair distribution, which is used to calculate upper limit on the mixing parameter of the U boson, is corrected by the acceptance and efficiency using curve presented in Fig. 5.27.

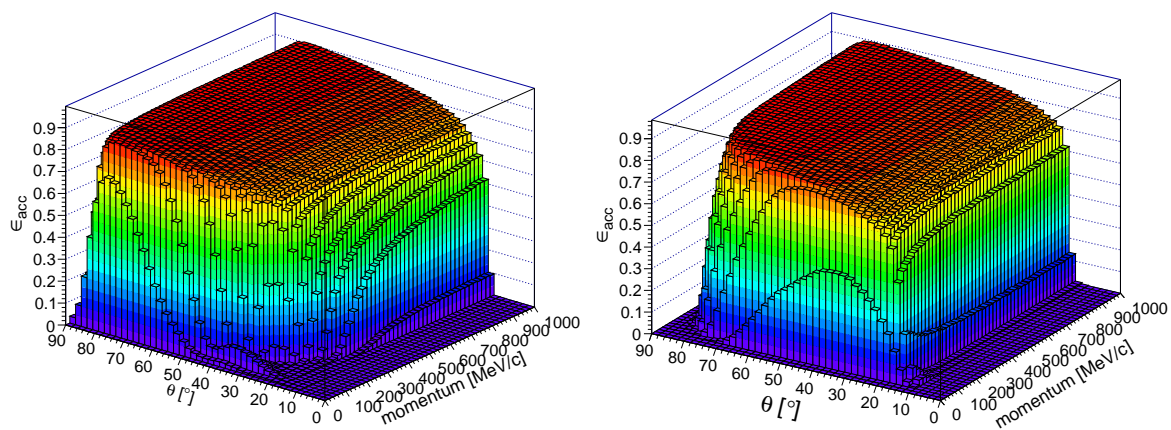


Figure 5.25: **Left:** Acceptance as a function of particle momentum and azimuthal angle for positrons (left) and electron (right).

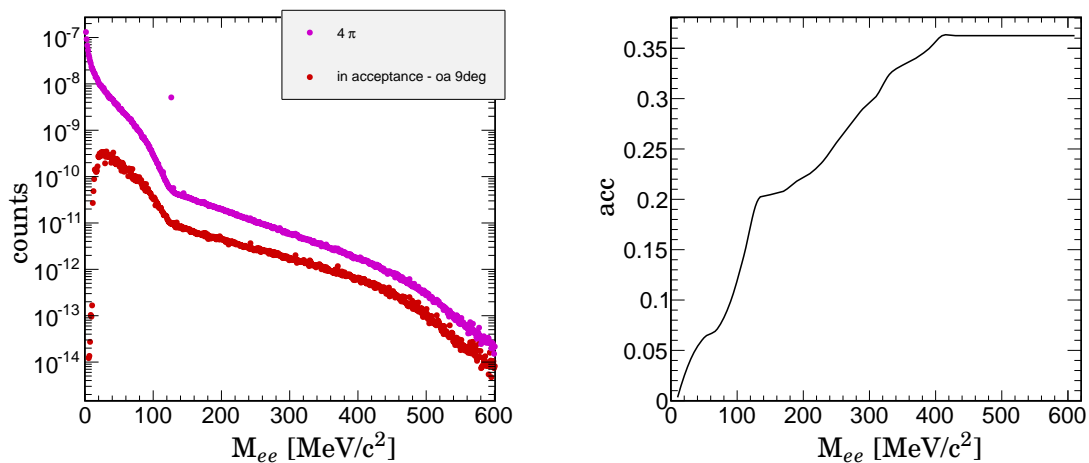


Figure 5.26: **Left:** Pluto cocktail in full phase space (lila circles) and in HADES acceptance with 9° opening angle cut (red circles). **Right:** Acceptance as a function of the invariant dilepton mass.

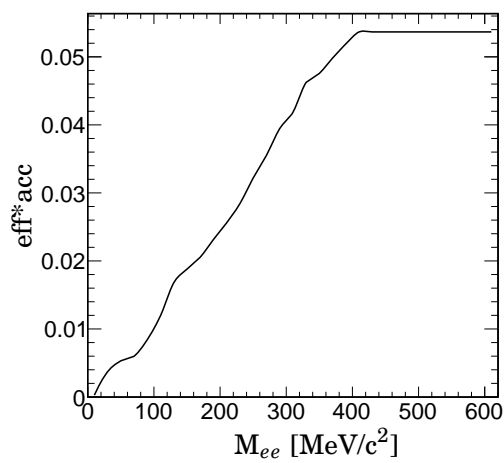


Figure 5.27: Acceptance times efficiency as a function of the invariant dilepton mass.

Chapter 6

Search for the Dark Photon

The U boson search is performed using the raw dilepton spectrum of unlike-sign lepton pairs as shown in Fig. 5.21. One has to mention here that the Au(1.23 AGeV) + Au data is analysed to get the upper limit on the mixing parameter ϵ further down. For this the invariant dilepton spectra of the p+p, p+Nb, Ar+KCl and Au+Au experiments should be compared, which is done in Fig. 6.1 (left panel). With respect to the rescaled Ar+KCl data, the Au+Au data has around

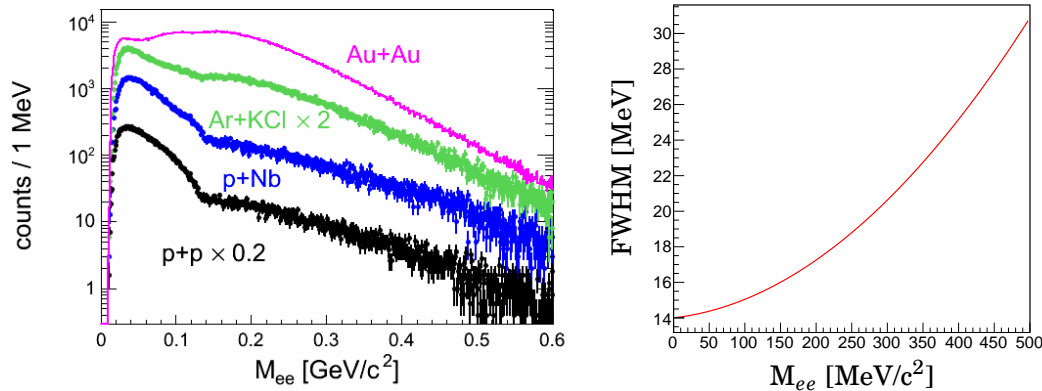


Figure 6.1: **Left:** Measured inclusive e^+e^- invariant-mass distributions for p+p and p+Nb at 3.5 GeV, as well as for 1.765 AGeV Ar+KCl and 1.23 AGeV Au+Au reactions in the HADES geometrical acceptance with single lepton momenta $p_e > 0.05$ GeV and pair opening angles $\theta_{e^+e^-} > 9^\circ$. **Right:** Dielectron mass resolution (FWHM) as a function of the e^+e^- invariant mass obtained from a GEANT3-based Monte-Carlo simulation.

factor of 4 more statistic than in Ar+KCl data. If one recalculates the total numbers of mesons (N_{π^0}) produced in these experiments one gets a factor of 6 more mesons recorded in the Au+Au data, see Tab. 6.1.

In contrast to the other experiments, which are mentioned in Chap. 2, HADES has measured the inclusive e^+e^- invariant-mass distribution. This means that the invariant mass distribution consists of a cocktail of contributions from different sources. One has to take into account the electromagnetic decay of $\pi^0 \rightarrow \gamma U$, $\eta \rightarrow \gamma U$ and $\Delta \rightarrow NU$, if one wants to search for the hypothetical U boson ($U \rightarrow e^+e^-$), that's why an irreducible background is always present. Due to the very similar decay kinematics of the Dalitz decays the different sources can not be discriminated from a possible U boson signal via analysis cuts. Therefore one has to search for a possible peak on a smooth varying continuum.

A possible signal of the U boson decay would be very sharp, because of the expected long life-

Reaction	N_{LVL1}	N_{π^0}
p+p	3.0×10^9	2.5×10^9
p+Nb	7.7×10^9	5.9×10^9
Ar+KCl	2.2×10^9	7.7×10^9
Au+Au	4.7×10^9	47.0×10^9

Table 6.1: Number of triggered events N_{LVL1} and total number of produced π^0 (N_{π^0}) in the HADES experiments [25].

time, and the width of the expected peak will be determined by the detector resolution. The mass resolution as a function of the invariant mass is presented in Fig. 6.1. It is obtained from a GEANT3-based Monte-Carlo simulation of e^+e^- decays detected in the HADES spectrometer. The mass resolution in the π^0 region is approximately 15 MeV and increases smoothly with invariant masses up to 30 MeV in the η region.

6.1 Determination of the Upper Limit

As mentioned previously in Chap. 4.6 the ROOT C++ based tool named TRolke (Sec. 4.6) is used to determine an upper limit on the mixing parameter. Therefore the raw dilepton spectrum is analysed in a range from 20 to 600 MeV/c², which is not corrected for efficiency and acceptance (Fig. 5.21).

In order to search for possible peak in the raw unlike-sign dilepton spectrum a 5th-order polynomial with a Gauss peak

$$f(m_{ee}) = a \cdot e^{-\frac{(m_{ee}-b)^2}{2c^2}} + d \cdot m_{ee}^5 + e \cdot m_{ee}^4 + f \cdot m_{ee}^3 + g \cdot m_{ee}^2 + h \cdot m_{ee} + i \quad (6.1)$$

is fit to the spectrum in a range of $2\sigma = \text{FWHM}/2.35$ (Fig. 6.1), where the variables a to i are fit parameters. The position and the width of the Gauss are fixed. Two fit examples are shown in Fig. 6.2. The Gauss fit has to be further controlled in order not to indicate a peak although there is no peak visible. The fits are done in 3 MeV steps and after fitting an integral of the polynomial background function is calculated in a range of 1.5σ . In addition one integrates over the raw dilepton spectrum in the same range. This analysis shows that no peak is present in our data. Now the statistical likelihood-based test must be performed in order to determine at a given confidence level (90%) an upper limit on the U boson. The so-called profile likelihood ratio is computed as a function of the signal strength S (integral data) together with a present so-called nuisance parameter, which is known as the estimated background yield (integral polynomial fit), the geometrical acceptance and the detector and reconstruction efficiency, see Fig. 5.27. All parameters are used as an input for the extended profile likelihood method, which is implemented in the ROOT framework as TRolke class, see sec. 4.6. For the background the acceptance and efficiency (acc×eff) corrections a gaussian error is assumed.

The resulting upper limit without any efficiency and acceptance correction expressed as detectable counts is presented in Fig. 6.3 for the mass range between 0.02 GeV/c² to 0.55 GeV/c². The expected sensitivity of our experiment is shown additionally. Therefore the upper limit is re-evaluated with the “zero-signal” hypothesis, i.e. assuming $S=0$, many times (10,000 iterations). After re-evaluation the median and the standard deviation of the generated upper limit is plotted as a function of the invariant mass together with the upper limit in Fig. 6.3. If the

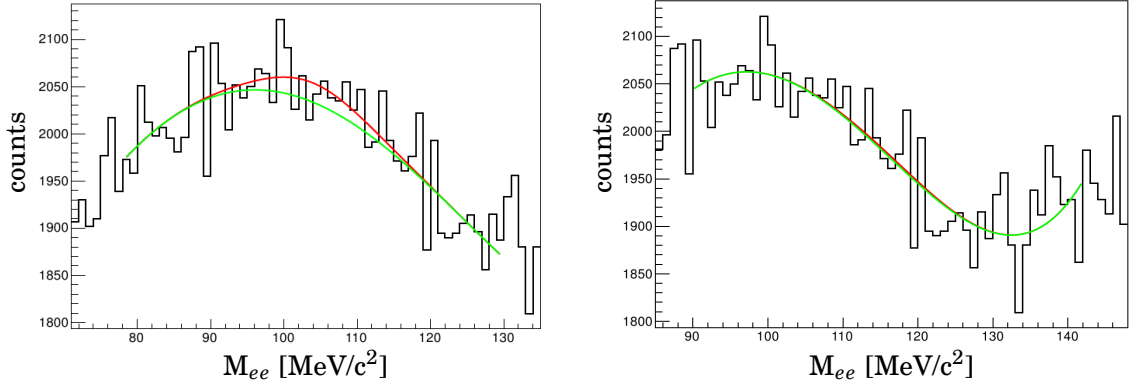


Figure 6.2: **Left:** 5th-order polynomial fit (green) with a gauss (red). **Right:** Correct polynomial (green) and gauss (red) fit. No peak is indicated.

upper limit is normal distributed, 68% (95%) of the data points should lie within the $\pm 1\sigma$ ($\pm 2\sigma$) band.

6.2 Upper Limit on ϵ^2

After correcting the median upper limit by the acc \times eff curve in Fig. 5.27, the upper limit on ϵ^2 has to be calculated.

As mentioned before, one has to take into account that HADES is measuring an inclusive dilepton spectrum. The measured dN/dM_{ee} distribution consists of a cocktail from different sources and the search for the U boson has to take this into account.

One can estimate the U boson yield by

$$N_U = \sum_i N_U^{(i)}, \quad (6.2)$$

where $N_U^{(i)}$ refers to different sources, like $i = \pi^0, \eta$ and Δ with a U boson instead of a virtual photon.

The ratio of widths can be obtained from data via

$$\frac{\Gamma_{i \rightarrow \gamma U}}{\Gamma_{i \rightarrow \gamma \gamma}} = \frac{N_U^{(i)}}{N_i BR_{i \rightarrow \gamma \gamma}}, \quad (6.3)$$

$$\frac{\Gamma_{\Delta \rightarrow NU}}{\Gamma_{\Delta \rightarrow N \gamma}} = \frac{N_U^\Delta}{N_\Delta BR_{\Delta \rightarrow N \gamma}}, \quad (6.4)$$

where $i = \pi^0$ and η . To arrive at ϵ^2 the expression

$$\frac{\Gamma_{i \rightarrow \gamma U}}{\Gamma_{i \rightarrow \gamma \gamma}} = 2\epsilon^2 |F_i(q^2 = M_U^2)| \frac{\lambda^{3/2}(m_i^2, m_\gamma^2, M_U^2)}{\lambda^{3/2}(m_i^2, m_\gamma^2, m_\gamma^2)} \quad (6.5)$$

can be used. λ is the standard triangle function for relativistic kinematics and $F_i(q^2)$ is the electromagnetic transition form factor. For on-shell photons ($m_\gamma^2 = 0$) one gets

$$\frac{\lambda^{3/2}(m_\eta^2, 0, M_U^2)}{\lambda^{3/2}(m_\eta^2, 0, 0)} = \left(1 - \frac{M_U^2}{m_\eta^2}\right)^3. \quad (6.6)$$

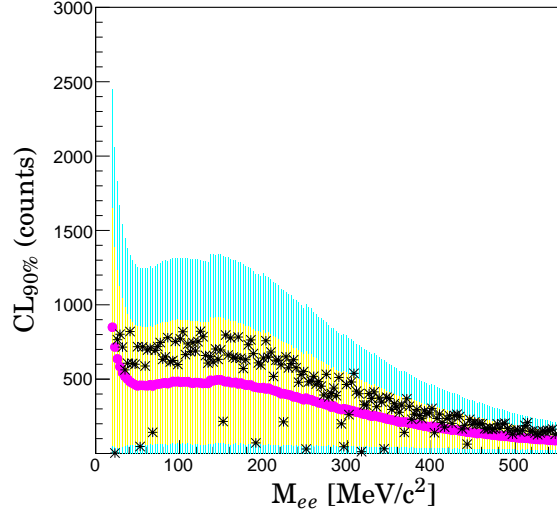


Figure 6.3: Upper limit on the U boson expressed as detectable counts as a function of the invariant mass. The computed experimental sensitivity (black points) is shown together with 1σ (yellow) and 2σ (blue) bands.

For Δ one has to mention that it is a broad state and the decay width $\Gamma_{\Delta \rightarrow NU}$ has to be averaged over the Δ mass distribution $A(m_\Delta)$, described by a Breit-Wigner shape of width $\Gamma = 117$ MeV. One gets the expression

$$\frac{\Gamma_{\Delta \rightarrow NU}}{\Gamma_{\Delta \rightarrow N\gamma}} = \epsilon^2 \int A(m_\Delta) |F_\Delta(M_U^2)| \frac{\lambda^{3/2}(m_\Delta^2, m_N^2, M_U^2)}{\lambda^{3/2}(m_\Delta^2, m_N^2, 0)} dm_\Delta. \quad (6.7)$$

Furthermore the η and Δ decays are giving access to masses larger than the $\mu^+\mu^-$ threshold at $2m_\mu = 0.21$ GeV/ c^2 , therefore the observed U boson signal has to be corrected for the branching fraction into e^+e^- , that is $BR_{ee} = BR_{U \rightarrow e^+e^-}$:

$$BR_{ee} = \Gamma_{ee} / \Gamma_{tot} = \frac{\Gamma_{ee}}{\Gamma_{ee} + \Gamma_{\mu\mu} + \Gamma_{had}} \quad (6.8)$$

For lepton universality one can write $\Gamma_{\mu\mu} = \Gamma_{ee}$ for $M_U \gg 2m_\mu$ and estimating the hadronic decay width by the factor $R(\sqrt{s}) = \sigma_{e^+e^- \rightarrow hadrons} / \sigma_{e^+e^- \rightarrow \mu^+\mu^-}$, so that $\Gamma_{had} = R(M_U) \Gamma_{\mu\mu}$, the branching relevant for the U boson search is expressed as

$$BR_{ee} = \frac{1}{1 + \sqrt{1 - \frac{4m_\mu^2}{M_U^2}} \left(1 + \frac{2m_\mu^2}{M_U^2}\right) [1 + R(M_U)]}. \quad (6.9)$$

In Fig. 6.4 the branching ratio BR_{ee} as a function of M_U is plotted. All together one obtains

$$\begin{aligned} N_{U \rightarrow ee} &= N_{U \rightarrow ee}^\eta + N_{U \rightarrow ee}^{\pi^0} + N_{U \rightarrow ee}^\Delta \\ &= \epsilon^2 BR_{ee} [2N_\eta BR_{\eta \rightarrow \gamma\gamma} |F_\eta|^2 (1 - M_U^2/m_\eta^2)^3 \\ &\quad + 2N_{\pi^0} BR_{\pi^0 \rightarrow \gamma\gamma} |F_{\pi^0}|^2 (1 - M_U^2/m_{\pi^0}^2)^3 \\ &\quad + N_\Delta BR_{\Delta \rightarrow N\gamma} \times \int A(m_\Delta) |F_\Delta(M_U^2)| \frac{\lambda^{3/2}(m_\Delta^2, m_N^2, M_U^2)}{\lambda^{3/2}(m_\Delta^2, m_N^2, 0)} dm_\Delta] \\ &= \epsilon^2 BR_{ee} L(M_U), \end{aligned} \quad (6.10)$$

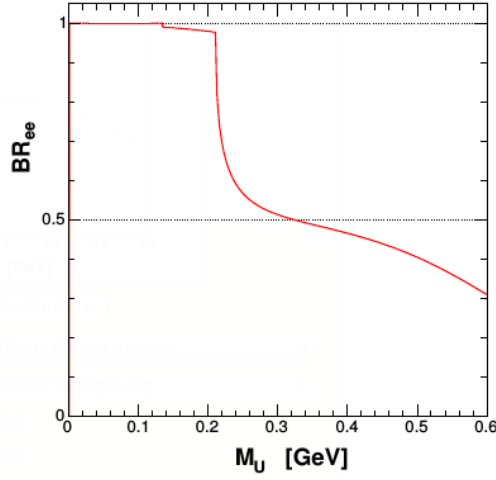


Figure 6.4: Branching ratio of the hypothetical U boson into an e^+e^- pair as a function of the U boson mass M_U , referring to Eq. 6.9 [25].

where $L(M_U)$ includes all kinematic factors and source parameters in Eq. 6.10.

If no signal of the U boson is found the obtained upper limit can be transformed into an upper limit on the mixing parameter ϵ^2 as a function of M_U . One has to mention that the calculations are based on the following assumptions:

- $i = \pi^0, \eta$ and Δ saturate the sum over all U boson sources,
- estimation of $BR_{U \rightarrow e^+e^-}$ is accurate enough for this purpose,
- the parameterisation of the transition form factor $|F_{\pi^0}(q^2)| = 1 + 0.032 q^2/m_{\pi^0}^2$ [54] and $|F_{\eta}(q^2)| = (1 - \frac{q^2}{\Lambda^2})^{-1}$ with $\Lambda = 0.72 \text{ GeV}$ [55] are sufficiently accurate
- the spectral distribution of Δ in Eq. 6.7 is correct
- the use of $|F_{\Delta}(q^2)| = 1$ is allowed, since an experimental form factor is not known
- uncertainties in the estimation of the Δ multiplicity by $N_{\Delta} = 3/2 N_{\pi^0}$ are of minor importance due to the small branching ratio $BR_{\Delta \rightarrow N\gamma} = 0.006$ in comparison with $BR_{\eta \rightarrow \gamma\gamma} = 0.393$ and $BR_{\pi^0 \rightarrow \gamma\gamma} = 0.988$ [54]

Chapter 7

Summary and Outlook

7.1 Summary

In this thesis the Au (1.23 AGeV) + Au data, which has been recorded in 2012, were analysed. In order to determine an upper limit on the U boson, first one had to identify leptons and reconstruct lepton pairs. For this purpose a multivariate analysis was used. It allows to apply a multidimensional cut on a particle sample. Compared to one dimensional cut on the sample one can gain in efficiency by using multidimensional cuts without losing purity. Therefore the neural network is trained with 9 variables for the RPC detector region and with 8 variables for the TOF detector. Afterwards a lepton identification cut on the MLP response larger than 0.6 was applied. For getting higher purity ($\sim 95\%$ for lower momenta ($p < 400 \text{ MeV}/c$)) of the lepton sample an additional cut on the ring matching quality ($\text{richQa} < 2$) was set.

For the determination of the lepton purity in the experimental data the rotated RICH detector method has been used. In the cross-check with the simulation data the efficiency and purity values have been verified.

After identifying single leptons an invariant mass spectrum is built containing all possible e^+e^- pairs, corrected by an acceptance and efficiency factor. The efficiency correction includes the particle detection reconstruction and identification efficiency. In the acceptance correction the coverage of the HADES spectrometer with respect to the full phase space is considered.

By using the method of TRolke, an upper limit with a confidence level of 90% on the U boson was calculated (see Fig. 6).

7.2 Outlook

The next step would be to calculate ϵ^2 as a function of the invariant dilepton mass in order to compare the obtaining result with the other experiments. Regarding the result of the NA48/2 Collaboration and the $(g-2)_{\mu}$ band, the result from the HADES data can be used to confirm the results of the other experiments by an independent measurement.

In order to get the upper limit further down by using the Au+Au data, one can further improve the lepton identification process. One opportunity would be to use the back tracking information, on which Patrick Sellheim from the HADES collaboration, is working on. The aim would be to get the same amount of purity by gaining in cutting efficiency. An other possibility would be to apply a momentum depend richQa or momentum depend MLP cut, to gain in statistic. For HADES the invariant mass region smaller than $100 \text{ MeV}/c^2$ is of interest for determine an upper limit or get it further down. In the mass range $M_{ee} > 100 \text{ MeV}/c^2$ other experiments are able to collect much more statistic.

List of Figures

2.1	The positron fraction measured by AMS (red circles) compared with the expectation from the collision of ordinary cosmic rays showing that above 8 billion electron volts (8 GeV) the positron fraction begins to quickly increase. This increase indicates the existence new sources of positrons [2].	11
2.2	Elementary particles and force carriers of the Standard Model.	12
2.3	Exclusion plot at 90% CL on e^2 as function of $m_{A'}$. The result from HADES [25] is compared with existing limits from the APEX [18], WASA-at-COSY [19], KLOE-2 [20, 21], BaBar [22], MAMI/A1 [26] and NA48/2 [23] experiments, as well as with the $(g - 2)_\mu$ and $(g-2)_e$ constraints.	14
3.1	The phase diagram of QCD including data points in T and μ_B describing the final hadron ratios in a statistical model. The hadrochemical freeze-out points are determined from a thermal model analysis of heavy-ion collision data at SIS, AGS, SPS and RHIC energies. The condensate ratio $\langle q\bar{q} \rangle_{T,\mu_B} / \langle q\bar{q} \rangle_{T=0,\mu_B=0}$ in dependence on T and μ_B is shown as 3rd dimension in color code. The condensate ratio is reduced for high T and μ_B as predicted by Nambu Jona Lasinio model [28].	16
3.2	Overview over the HADES spectrometer [31].	16
3.3	Cross-section of the HADES with the different detector components shown [33].	17
3.4	Schematic view of the start and veto detector [35].	18
3.5	Schematic layout of the RICH, consisting of a carbon shell mirror, a CaF ₂ entrance window and a photon detector. All distances are in millimeter [33].	18
3.6	Schematic view of the six anode wire frames inside a MDC [33].	19
3.7	Momentum-dependent dE/dx distribution (normalized) measured by MDC. Energy loss curves of several hadron species are calculated by Bethe-Bloch formula (Eq. 3.1) and plotted into distribution [29].	19
3.8	Left: Energy loss vs. momentum distribution in TOF region with identified particles. Right: β vs. momentum distribution for TOF region with identified particles.	20
3.9	Left: Schematic view of the electromagnetic shower algorithm. In each layer the charge over the 3x3 pads is integrated. The large charge deposition in the post chambers is the signature of an electromagnetic shower [33]. Right: Schematic layout of the Pre-Shower detector [37].	21
3.10	Pre-Shower signal of leptons (left) and hadrons (right).	22
3.11	Recorded raw data as a function of the beam on target for different experiments.	22
3.12	The HADES data for the p (3.5 GeV) + p \rightarrow e ⁺ e ⁻ X reaction from 2007, compared to a simulated cocktail from the PYTHIA event generator [43].	24

4.1	RICH matching quality (richQa) as a function of momentum based on the experimental data in RPC and TOF region.	26
4.2	Architecture of the neural network used for the Au+Au data analysis in the region of the RPC detector. Shown are couplings between the neurons of the input layer (0), the two hidden layers (1,2) and the output layer.	28
4.3	Architecture of the neural network used for the Au+Au data analysis in the region of the TOF detector. Shown are couplings between the neurons of the input layer (0), the two hidden layers (1,2) and the output layer.	28
5.1	Total number of registered events in the Au+Au beamtime in 2012 after PT3 trigger and at least one registered hit in start or veto detector.	31
5.2	Upper row: β versus momentum for RPC (left) and TOF (right) region. Lower row: Response of the MLP network for RPC (left) and TOF (right) region.	33
5.3	Upper row: Correlation matrix in the RPC region. The values are representing the correlation of two variables in percent. Lower row: Correlation matrix in the TOF region. Boxes without values have correlations close to 0.	34
5.4	Signal and background distribution for each input variable separately in the RPC region.	35
5.5	Signal and background distribution for each input variable separately in the TOF region.	36
5.6	β versus momentum distribution after applying richQa $< 2^\circ$ and MLP > 0.6 . The shape of all five distributions looks the same. A cut on $\beta > 0.9$ is applied already on the pre-selection level.	37
5.7	The HADES spectrometer is built up of six sectors. In the “rotated RICH detector method” the RICH detector is rotated software-wise by 60° . After rotation the MDC sector and the RICH sector is shifted by one sector clockwise.	38
5.8	Momentum distribution without ID cut (red curve) and for different cases. The distributions without ID cut are contaminated by hadrons at $p > 200$ MeV/c. Case 0 and 2 coincide, whereas case 1 has less leptons left after applying both cuts (richQa $< 2^\circ$ & MLP > 0.6) to the three different cases.	38
5.9	Percentage values of background in the lepton sample as a function of momentum in experimental data. Case 1, in which no θ is included and where deposited charge in the shower detector is divided by the momentum, shows the worst percentage values. The amount of wrongly matched tracks is higher than in case 0 and 2. For case 0 (with θ and case 2 (no θ) the amount of background is in the same order.	39
5.10	β versus momentum distribution for RPC and TOF region without any particle identification cut. The integral of the distribution is shown in the top right corner. Left column: Without asking for the GeantPID number (all particles). Middle column: Asking for GeantPID of leptons. Right column: Asking for GeantPID of hadrons.	40
5.11	Percentage values of purity and efficiency in the TOF (right panel) and RPC (left panel) regions. Efficiency for hadrons is of the order of 10^{-3} to 10^{-4} and can not be displayed in the same chart. A particle identification cut of MLP > 0.6 is applied.	41

5.12	Percentage values of purity and efficiency in the TOF (right panel) and RPC (left panel) region. Efficiency for hadrons is of the order of 10^{-3} to 10^{-4} and can not be displayed in the same chart. Particle identification cuts of $MLP > 0.6$ and $richQa < 2^\circ$ are applied.	42
5.13	β versus momentum distribution for RPC and TOF region after a particle identification cut $MLP > 0.6$. The integrals of the distribution are shown in the top right corners.	42
5.14	β versus momentum distribution in the RPC and TOF regions after particle identification cuts $MLP > 0.6$ & $richQa < 2^\circ$. The integrals of the distribution are shown in the top right corners.	43
5.15	Polar angle θ as a function of the the metaQa*polarity value. Left column: Without any cut and plotted for all particles. Right column: Same distribution but after applying lepton identification cuts: $RichQa < 2$, effective mass < 90 MeV/c ²	44
5.16	Upper panel: Characterization of the dx distribution for all the scintillator cells for negative pions with a momentum between 500-600 MeV/c. In the left are plotted the residuals, in the center the RMS and in the right panel the scattered plot with the first panels together. Lower panel: Same as upper but for simulated data.	45
5.17	Left column: META dx versus β distribution for one cell of the TOF detector. Right column: Mean of the gaussian dx distribution calculated for one cell dependent on β , error bars are the gaussian sigma of the distribution.	46
5.18	Left column: dx mean value obtained from the 2D distribution (right column). Middle column: RMS value calculated from the 2D distribution. Right column: Corrected META dx versus cell number distribution plotted for the TOF detector together with mean and RMS.	46
5.19	Upper panel: θ distribution for cuts on $metaQa = \sqrt{\frac{dx}{\delta dx}^2 + \frac{dy}{\delta dy}^2}$ (left column) and cuts on the new $metaQa' = \left \frac{dx}{\sigma(dx)} \right $ (right column). Lower panel: Same analysis applied to the rapidity distribution.	47
5.20	Left: Opening angle distribution for different lepton pair sources [27]. Right: Comparison between the unlike-sign lepton pair distribution with and without opening angle cut ($\alpha < 9^\circ$).	49
5.21	Left: $N_{e^+e^-}$, $N_{e^+e^+}$ and $N_{e^-e^-}$ distributions with an opening angle cut of $\alpha < 9^\circ$. Right: $N_{e^+e^-}$ (yellow squares) distribution together with the combinatorial background $CB_{e^+e^-}$ (blue circles) and the signal distribution $S_{e^+e^-}$ (green triangle).	51
5.22	Left: Uncorrected (yellow squares) and corrected (blue circles) unlike-sign dilepton spectrum with an opening angle cut of 9° . Right: Efficiency correction factor as a function of invariant mass.	51
5.23	Positron reconstruction efficiency as a function of θ and momentum, averaged over all ϕ 's for every sector separately.	52
5.24	Left: Cocktail simulated with event generator Pluto [53] in full phase space. Right: Pluto cocktail inside HADES acceptance and with 9° opening angle cut.	53
5.25	Left: Acceptance as a function of particle momentum and azimuthal angle for positrons (left) and electron (right).	54
5.26	Left: Pluto cocktail in full phase space (lila circles) and in HADES acceptance with 9° opening angle cut (red circles). Right: Acceptance as a function of the invariant dilepton mass.	54

5.27	Acceptance times efficiency as a function of the invariant dilepton mass.	55
6.1	Left: Measured inclusive e^+e^- invariant-mass distributions for p+p and p+Nb at 3.5 GeV, as well as for 1.765 AGeV Ar+KCl and 1.23 AGeV Au+Au reactions in the HADES geometrical acceptance with single lepton momenta $p_e > 0.05$ GeV and pair opening angles $\theta_{e^+e^-} > 9^\circ$. Right: Dielectron mass resolution (FWHM) as a function of the e^+e^- invariant mass obtained from a GEANT3-based Monte-Carlo simulation.	57
6.2	Left: 5^{th} -order polynomial fit (green) with a gauss (red). Right: Correct polynomial (green) and gauss (red) fit. No peak is indicated.	59
6.3	Upper limit on the U boson expressed as detectable counts as a function of the invariant mass. The computed experimental sensitivity (black points) is shown together with 1σ (yellow) and 2σ (blue) bands.	60
6.4	Branching ratio of the hypothetical U boson into an e^+e^- pair as a function of the U boson mass M_U , referring to Eq. 6.9 [25].	61

List of Tables

3.1	Characteristic quantities of light vector mesons [29].	15
3.2	This list of experiments with different collision systems and beam energies have been conducted using the HADES spectrometer. The number of events recorded is shown. The number of LVL1 triggers is given [34].	23
5.1	Overview over all variables included for the training and testing of the neural network.	33
6.1	Number of triggered events N_{LVL1} and total number of produced π^0 (N_{π^0}) in the HADES experiments [25].	58

Bibliography

- [1] Hinshaw, G. *et al.*, “*Nine-Year Wilkinson Microwave Anisotropy Probe (WMAP) Observations*”, *ApJS.*, 208, 20B (2013).
- [2] AMS-02 collaboration, “*New results from the Alpha Magnetic Spectrometer on the International Space Station*”, <http://www.ams02.org/> (2014).
- [3] Jean, P. *et al.*, *Astron. Astrophys.* 407, L55 (2003).
- [4] Adriani, O. *et al.*, “*An anomalous positron abundance in cosmic rays*”, *Nature (London)*, 458, 607 (2009).
- [5] Aguilar, M. *et al.* (AMS Collaboration), “*First Result from the Alpha Magnetic Spectrometer ...*”, *Phys.Rev.Lett.* 110, 141102 (2013).
- [6] Fazely, A.R. *et al.*, “*Cosmic Ray Proton Background Could Explain ATIC Electron Excess*”, arXiv:0904.2371v4 (2009).
- [7] Ackermann, M. *et al.*, “*Measurement of Separate Cosmic-Ray Electron and Positron Spectra*”, *Phys. Rev. Lett.* 108, 011103 (2012).
- [8] Aharonian, F. *et al.*, “*Probing the ATIC peak in the cosmic-ray electron spectrum with H.E.S.S.*”, *Astron. Astrophys.* 508, 561 (2009).
- [9] Bernabei, R. *et al.*, “*First results from DAMA/LIBRA and the combined results with DAMA/NaI*”, *Eur.Phys.J.C*56:333-355 (2008).
- [10] Holdom, B. *et al.*, “*Two $U(1)$'s and e charge shifts*”, *Phys. Lett.* B1 196 (1986).
- [11] The CMS Collaboration, “*Observation of a new boson at a mass of 125 GeV with the CMS experiment at the LHC*”, *Phys.Lett.* B 716 (2012).
- [12] Holdom, B. *et al.* (ATLAS Collaboration), “*Observation of a new particle in the search for the Standard Model Higgs boson with the ATLAS detector at the LHC*”, *Phys.Lett.* B 716 (2012).
- [13] Herrero, M.J., “*The Standard Model*”, arXiv:hep-ph/9812242 (1998).
- [14] The BaBar Collaboration and Soffer, A., “*Constraints on dark forces from the B factories and low-energy experiments*”, arXiv:1409.5263 (2014).
- [15] Arkani-Hamed, N. *et al.*, “*A Theory of Dark Matter*”, *Phys. Rev. D* 79, 015014 (2009).
- [16] Bjorken, J. *et al.*, “*New fixed-target experiments to search for dark gauge forces*”, *Phys. Rev. D* 80, 075018 (2009).
- [17] Merkel, H. *et al.* (A1 Collaboration), “*Search for Light Gauge Bosons of the Dark Sector at the Mainz Microtron*”, *Phys. Rev. Lett.* 106, 251802 (2011).
- [18] Abrahamyan, S. *et al.* (APEX Collaboration), “*Search for a New Gauge Boson in Electron-Nucleus Fixed-Target Scattering*”, *Phys. Rev. Lett.* 107, 191804 (2011).

- [19] Adlarson, P. *et al.* (WASA-at-COSY Collaboration), “*Search for a dark photon in the π^0 decay*”, Phys. Lett. B 726, 187 (2013).
- [20] Archilli, F. *et al.* (KLOE-2 collaboration), “*Search for a vector gauge boson in phi meson decays*”, Phys. Lett. B 706, 251 (2012).
- [21] Babuski, D. *et al.* (KLOE-2 collaboration), “*Limit on the production of a light vector gauge boson in phi meson decays*”, Phys. Lett. B 720, 111 (2013).
- [22] Lees, J.P. *et al.*, “*Search for a dark photon in e^+e^- collisions at BABAR.*”, Phys Rev Lett. 113, 20, 201801 (2014).
- [23] NA48/2 collaboration and Goudzovski, E., “*Search for the dark photon in π^0 decays by the NA48/2 experiment at CERN*”, arXiv:1412.8053 (2014).
- [24] Hoecker, A. and Marciano, W.J., “*The muon anomalous magnetic moment*”, Phys. Rev. D 86, 010001 (2011).
- [25] Agakishiev, G. *et al.* (Hades Collaboration), “*Searching a Dark Photon with HADES*”, Phys. Lett. B 731 (2013).
- [26] Merkel, H. *et al.* (A1 Collaboration), “*Search for light massive gauge bosons at MAMI*”, Phys. Rev. Lett. 112, 221802 (2014).
- [27] Sudol, M., “*Mesaurement of low-mass e^+e^- pair production in 2 AGeV C-C collisions with HADES*”, PhD thesis (2007).
- [28] Galatyuk, T. *et al.* (HADES Collaboration), Nucl.Phys. A931 41-51 (2014).
- [29] Olive, K.A. *et al.*, “*Review of particle physics 2014*”, Chin. Phys. C38, 090001 (2014).
- [30] Borsanyi, S. *et al.*, “*Recent results on QCD thermodynamics: lattice QCD versus Hadron Resonance Gas model*”, JHEP 1009:073 (2010).
- [31] Schmah, A., “*In Vorbereitung: Strangeness Produktion in Ar+KCl Reaktionen bei 1.756 AGeV.*”, PhD thesis (2008).
- [32] GSI, “*Ringbeschleuniger SIS18*”, <https://www.gsi.de/> (2015).
- [33] Agakishiev, G. *et al.* (HADES Collaboration), “*The High-Acceptance Dielectron Spectrometer HADES*”, Eur.Phys.J.A 41, 243–277 (2009).
- [34] Michel, J., “*Development and Implementation of a New Trigger and Data Acquisition System for the HADES Detector*”, PhD thesis (2012).
- [35] Pietraszko, J. *et al.*, Nucl.Instrum.Meth. A763 (2014).
- [36] Zeitelhack, K. *et al.*, “*The HADES RICH detector*”, Nuclear Instruments and Methods in Physics Research A 433, 201–206 (1999).
- [37] Manuel, L., “*Vector meson production in p+Nb reactions and statistical particle production in Ar+KCl collisions*”, PhD thesis (2012).
- [38] Andreeva, O.V. *et al.*, Instrum. Exp. Tech. 57, 103–119 (2014).
- [39] Matis, H.S. *et al.* (DLS Collaboration), Nucl.Phys.A583:617C-622C (1995).
- [40] Hades Collaboration and Agakishiev, G. *et al.*, “*Dielectron production in Ar+KCl collisions at 1.76A GeV*”, Phys.Rev.C 84, 014902 (2011).
- [41] Agakishiev, G. *et al.* (HADES Collaboration), “*Inclusive pion and eta production in p+Nb collisions at 3.5 GeV beam energy*”, Phys. Rev. C 88, 024904 (2013).

-
- [42] Przygoda, W. *et al.* (DLS Collaboration), “*Hades experiment: di-lepton spectroscopy in $p+p$ (2.2 GeV) and $C+C$ (1 AND 2 AGeV) collisions*”, Acta Physica Polonica B37, 139 (2006).
- [43] Teilab, K. *et al.* (HADES Collaboration), “*Omega and eta meson production in $p+p$ reactions at $E_{kin} = 3.5$ GeV.*”, Int.J.Mod.Phys.A26, 694–696 (2010).
- [44] ROOT, “*An Object orientated Data Analysis Framework*”, <http://root.cern.ch/> (2004).
- [45] Froehlich, T. *et al.*, J. Phys. Conf. Ser. 219, 032039.
- [46] HGEANT, HADES Simulation Package, <http://www-hades.gsi.de/>.
- [47] Bass, S.A. *et al.*, Prog. Part. Nucl. Phys. 41, 225–370 (1998).
- [48] GEANT, “*Detector Description and Simulation Tool*, <http://consult.cern.ch/writeup/geant/>, *Online User Guide*”,
- [49] HYDRA, “*HADES analysis package*”, <http://www-hades.gsi.de/> (2004).
- [50] Oracle coporation, “*500 Oracle Parkway, Redwood Shores*”, CA 94065, USA.
- [51] Hoecker, A. *et al.*, “*TMVA 4 Users Guide*”, PoS ACAT: 040 (2013).
- [52] Lundberg, J. *et al.*, “*Limits, discovery and cut optimization for a Poisson process with uncertainty in background and signal efficiency: TRolke 2.0*”, Comput.Phys.Commun. **181**, 683–686 (2009).
- [53] Kagarlis, M.A., “*Pluto++*”, GSI Report (2000-2003).
- [54] Behringer, J. *et al.* (Particle Data Group), Phys. Rev. D 86, 010001 (2012).
- [55] Berghaeuser, H. *et al.*, Phys. Lett. B 701, 562 (2011).

Acknowledgements

My very special thanks I would like to express to my supervisor JProf. Dr. Tetyana Galatyuk and to Dr. Malgorzata Gumberidze, who guided my work during all stages of the master thesis. Their very broad experience, help and suggestions were absolutely crucial for me in carrying out this work.

Furthermore it has been a wonderful experience to work within the HADES collaborations. However it is difficult to recall every person that has assisted, contributed or more importantly encouraged me to pursue these studies. I would like to acknowledge all my colleagues from GSI, people of the HADES collaboration and my colleagues from the ViP-QM group from TU Darmstadt: Szymon Harabasz, Dr. Georgy Kornakov.

Thank you, my family, for encouraging me so much in life and helped me become the person I am today. I am proud that I belong to you and that you belong to me; I love you all more than I have words to express. Thank you, for your special charm.

On the end i would like to thanks friends for the support during my life and whole time at the university. I have to be so grateful to have you as my friends.

Erklärung zur Master-Thesis

Hiermit versichere ich die vorliegende Master-Thesis ohne Hilfe Dritter nur mit den angegebenen Quellen und Hilfsmitteln angefertigt zu haben. Alle Stellen, die aus Quellen entnommen wurden, sind als solche kenntlich gemacht. Diese Arbeit hat in gleicher oder ähnlicher Form noch keiner Prüfungsbehörde vorgelegen.

Ort, Datum

Unterschrift